Molecular Dynamics Studies of Anisotropy in Grain Boundary Energy and Mobility in UO_2

Jarin C. French

Thesis submitted to the faculty of the Virginia Polytechnic Institute and State University in partial fulfillment of the requirements for the degree of

Master of Science

in

Materials Science and Engineering

Xian-Ming (David) Bai, Chair

Sean G. Corcoran

Wenjun (Rebecca) Cai

25 April 2019

Blacksburg, Virginia

Keywords: Grain boundary energy, grain boundary mobility, anisotropy, uranium dioxide, molecular dynamics

Molecular Dynamics Studies of Anisotropy in Grain Boundary Energy and Mobility in UO_2

Jarin C. French

Abstract

Nuclear energy is a proven large-scale, emission-free, around-the-clock energy source. As part of improving the nuclear energy efficiency and safety, a significant amount of effort is being expended to understand how the microstructural evolution of nuclear fuels affects the overall fuel performance. Grain growth is an important aspect of microstructural evolution in nuclear fuels because grain size can affect many fuel performance properties. In this work, the anisotropy of grain boundary energy and mobility, which are two important properties for grain growth, is examined for the light water reactor fuel uranium dioxide (UO_2) by molecular dynamics simulations. The dependence of these properties on both misorientation angle and rotation axis is studied. The anisotropy in grain boundary energy is found to be insignificant in UO_2. However, grain boundary mobility shows significant anisotropy. For both 20º and 45º misorientation angles, the anisotropy in grain boundary mobility follows a trend of $M_{111} > M_{100} > M_{110}$, consistent with previous experimental results of face-centered-cubic metals. Evidences of grain rotation during grain growth are presented. The rotation behavior is found to be very complex: counterclockwise, clockwise, and no rotation are all observed.

Molecular Dynamics Studies of Anisotropy in Grain Boundary Energy and Mobility in UO_2

Jarin C. French

General Audience Abstract

Energy needs in the world increase year after year. As part of the effort to address these increasing needs, an increasing effort is needed to study each aspect of energy generation. For energy generated via nuclear fission, i.e., nuclear energy, many things need to be understood to gain maximum efficiency with maximum safety. At the core of a nuclear reactor, transport of energy generated by nuclear fission is heavily dependent on the microscopic structure (microstructure) of the materials being used as fuel. Thus, this work examines the microstructure of the most common nuclear fuel, uranium dioxide (UO_2). The microstructure changes based on at least two properties: grain boundary energy, and grain boundary mobility. This work examines how these properties change based on the orientation of individual crystallites within the polycrystalline material. An additional aspect of microstructural evolution, namely grain rotation, is briefly discussed.

Acknowledgements

I acknowledge the financial support from the Nuclear Energy University Program and the Integrated University Program Fellowship provided by the Office of Nuclear Energy of the U.S. Department of Energy.

I acknowledge the Advanced Research Computing at Virginia Tech and the High Performance Computing Facilities at Idaho National Laboratory for providing computational resources and technical support that are critical for producing the results reported within this thesis.

Special thanks goes to my fellow group members: Yaxuan, Xiqi, Weiming, Fengai, and Axel. Their insights and discussions have helped me as I have worked on this research. Additionally, I would like to thank my advisor, Dr. Bai. His constructive criticism has helped me learn how to clearly articulate my ideas, and back them up with data.

Finally, I would like to thank my wife, Katrina. She has stood by me and supported me through this endeavor, continually encouraging me to do the best that I can.

Table of Contents

List of Figures

List of Tables

Chapter 1 - INTRODUCTION

Worldwide energy needs continue to increase year after year. The United States Energy Information Administration predicts that energy use worldwide will increase 28% by 2040 [1]. To meet this ever-increasing energy need, various energy-production methods (i.e. solar, wind, geothermal, coal and oil, etc.) have been developed and improved to increase efficiency and productivity. As climate change has become a significant concern to the world community, emission-free energy sources have become a primary focus. One emission-free energy source is nuclear power. Nuclear energy currently generates approximately 11% of the world's electricity [2]. Within the United States alone, nearly 20% of the electricity generated is through nuclear reactors [3]. As energy needs continue to grow, it becomes increasingly important to develop high-productivity energy systems that can meet those needs. Nuclear energy is unique among the various emission-free energy sources in that it can constantly generate energy. Other energy forms (i.e. solar and wind) are limited by external factors beyond direct control. Thus, nuclear energy is uniquely positioned to handle current and future energy needs.

Nuclear energy is generated primarily through the process of fission. This process occurs when a large nucleus (i.e. uranium) splits (either spontaneously or due to bombardment from neutrons). The combined mass of the fission products will not add up to the mass of the original nucleus. This missing mass has been converted to energy via Einstein's equation, $E = mc^2$. Figure 1 shows a schematic of the fission process. A single fission event will generate roughly 200 MeV [4]. To put this in perspective, a single 60-Watt lightbulb would need roughly 6,700 *trillion* (~6.7×10^{15}) fission events to run the bulb for one hour. One gram of fissile uranium (U-235) contains 6.02×10^{23} fissile nuclei. If each U-235 atom underwent fission, and the resulting energy was extracted with 100% efficiency, enough energy would be generated to power one lightbulb for nearly 90 million hours, or over 10,000 *years*. Typical efficiencies for nuclear reactors are around 35% [5], which would lower the estimate in this example to over 3,500 years. Nuclear fuel does not contain 100% fissile uranium however. Naturally occurring uranium is primarily made up of U-238 (over 99%), while fissile uranium (U-235) is approximately 0.7% of the total mass. Therefore, one gram of naturally occurring uranium would theoretically power a 60-Watt lightbulb for approximately 25 years (if all the U-235 underwent fission, and the

efficiency was 35%, see Ref. [6]). The amount of energy available in such a relatively simple procedure has great potential to address energy needs for many years to come.

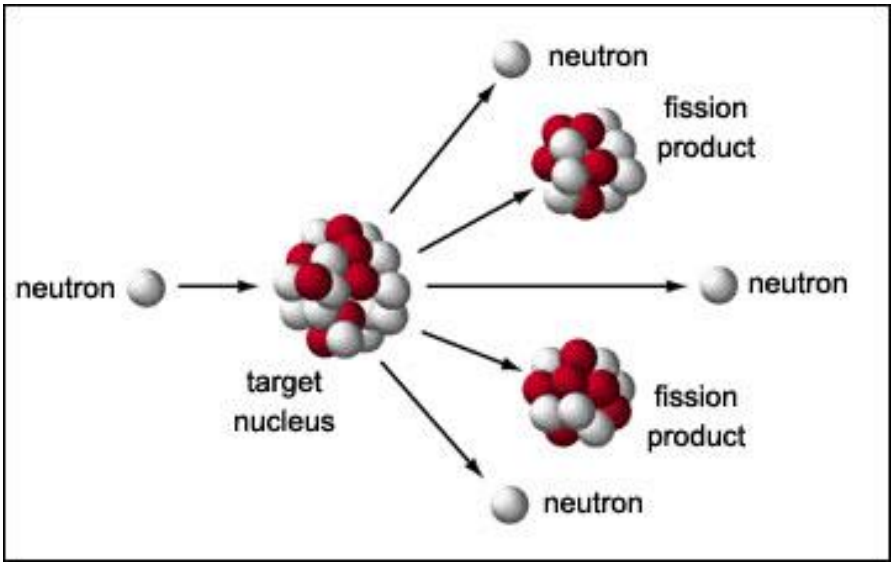

Figure 1 Schematic of the fission process. From Nuclear Fission Basics by atomicarchive.com. Copyright © 2019 by atomicarchive.com. Used with permission.

A schematic of a typical fission reactor is shown in Figure 2. The energy from the fission events is extracted as heat into a coolant (such as water). This heated coolant is then put through an exchanger to convert the heat into electricity. If the fission rate is too slow, the reactions will stop. Conversely, if the fission rate is too high, the reactor core may begin to melt. This can cause the coolant to be contaminated, and can eventually lead to total reactor meltdown if not quickly addressed. To control the rate at which fission events occur, a safety feature called control rods are used. These rods are made of neutron-absorbing materials so that fewer neutrons are available to contribute to the fission process. If the fission rate is too high, control rods are lowered into the reactor core to slow it down; they are raised if the fission rate is too low.

As part of the ongoing effort to address energy needs in a cleaner way, different nuclear fuels and reactor designs are being studied and developed. In the past, fuel-performance models were developed as a function of fuel burn-up (a measure of the energy extracted from the fuel). This approach has been identified as limited due to the specific conditions that such models were fit to [7]. Recent research efforts have been directed towards a microstructure-based approach, which requires accurate models of properties and behaviors across a wide range of conditions

[7]. Such an approach is limited only by the conditions used in the individual properties and behaviors, making development of such a model ideal for testing and designing improved fuels and reactors. Safety concerns limit the number and type of experiments that can be performed. This is where computer simulation plays an important role. Researchers at Idaho National Laboratory (INL) have developed a multi-physics framework called MOOSE (Multiphysics Object Oriented Simulation Environment) that can simulate processes at multiple time and length scales [8]. Using this framework, different 'animals' have been created, such as MARMOT (a nuclear materials phase-field and mechanics application) [9] and BISON (a fuel performance code) [10]. Used in concert with atomistic simulation, researchers are able to gain a clearer idea of the properties and behaviors of different fuels over picosecond timescales (i.e. radiation damage), as well as over yearlong timescales (i.e. creep and crack propagation).

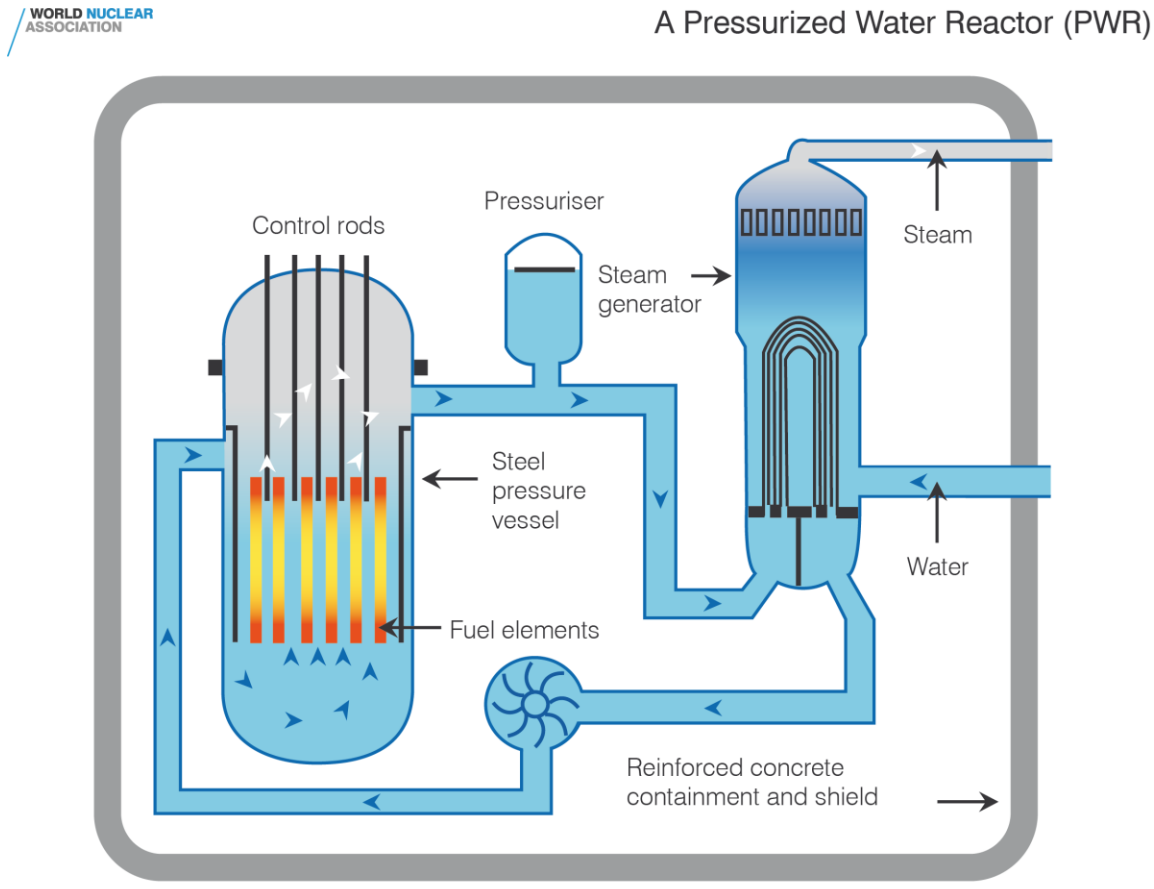

Figure 2 Schematic of a pressurized water reactor. From World Nuclear Association by world-nuclear.org. Copyright © 2019 by World Nuclear Association. Used with permission.

The fuel that has received the most attention from the research community is uranium dioxide (UO_2), which is the primary fuel source of current light water reactors (commercial reactors). UO_2 has the fluorite crystal structure, which consists of a face-centered cubic (fcc) lattice for the cations (uranium (U) atoms), while the anions (oxygen (O) atoms) are located at the eight tetrahedral sites, forming a simple cubic sub-lattice (see Figure 3). This material has been studied extensively, yet there are still many unanswered questions regarding how microstructural evolution affects its properties. It is a well-established fact that fuel performance properties (such as fission gas release, thermal conductivity, etc.) will change based on the microstructural evolution of the fuel, though accurate models describing these relationships are sparse. One method of quantifying these relationships is through an empirical comparison of the properties with the burn-up of the fuel. Burn-up is a measure of the amount of energy extracted per unit weight of fuel. Experimental works have examined fission gas release [11-13] and thermal transport [13, 14] in UO_2 as a function of burn-up. Their findings are indicative of an important relationship between microstructure (and its evolution) and the material properties of the fuel.

As UO_2 undergoes irradiation in reactors, a complex microstructural change occurs which forms a *high burn-up* structure (HBS) in the rim region of a fuel pellet, an example of which is shown in Figure 4. The HBS is characterized by a porous region of the microstructure with a small grain size. How this structure forms is still under debate, but increased pore pressure [15] and the formation of low-angle grain boundaries [16] are indicators of the development of the structure. Noirot *et al*. identified two additional potential markers for the development of this structure: the formation of planar defects, and an increase in the amount of local fission products [17]. Rondinella and Wiss [18] argued that the HBS forms because it minimizes the system free energy in a way that addresses the extreme environmental conditions the fuel experiences. The formation of the HBS is important to understand because of the effects it has on the fuel performance. Yuda *et al*. [19] identified that large-grained microstructures will decrease the amount of fission gas released (see also Refs. [11, 12]). Another impact of the development of the HBS studied by Terrani *et al*. [20] is that the Young's modulus is locally weakened with the formation of the HBS, which could play a role in fuel rod swelling. Swelling behavior occurs due primarily to both vacancy accumulation [21] (i.e. pores) and bubble coalescence [22]. Additionally, Turnbull and Friskney [23] identified a potential relationship between fuel rod

swelling and both grain size and grain size distribution. These works show that microstructural evolution (such as the formation of the HBS) has far-reaching effects on fuel performance properties. Because of the complex microstructure, and the material properties and behaviors that contribute to its evolution, much work remains to be done to accurately model UO_2 during its time in-reactor.

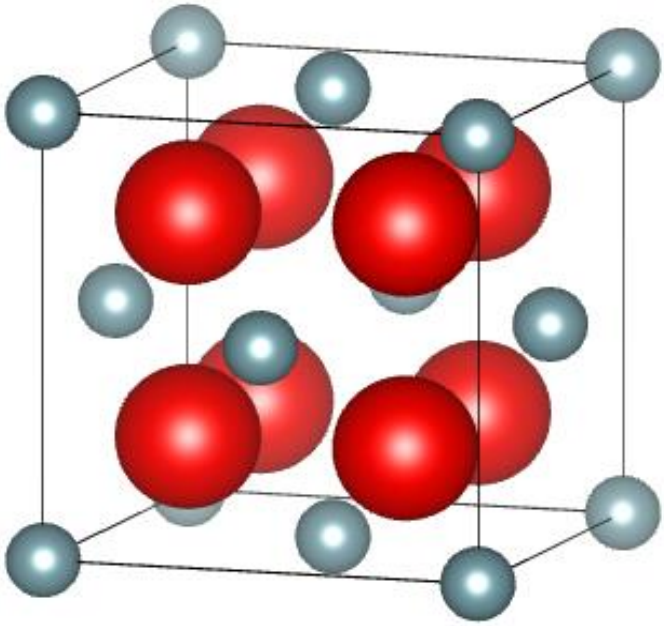

Figure 3 Schematic of the UO_2 structure. Image created using the VESTA [24] software. Uranium atoms (small, grey) are found on fcc points of the cube, and oxygen atoms (large, red) are found at the tetrahedral sites, forming a simple cubic sub-lattice.

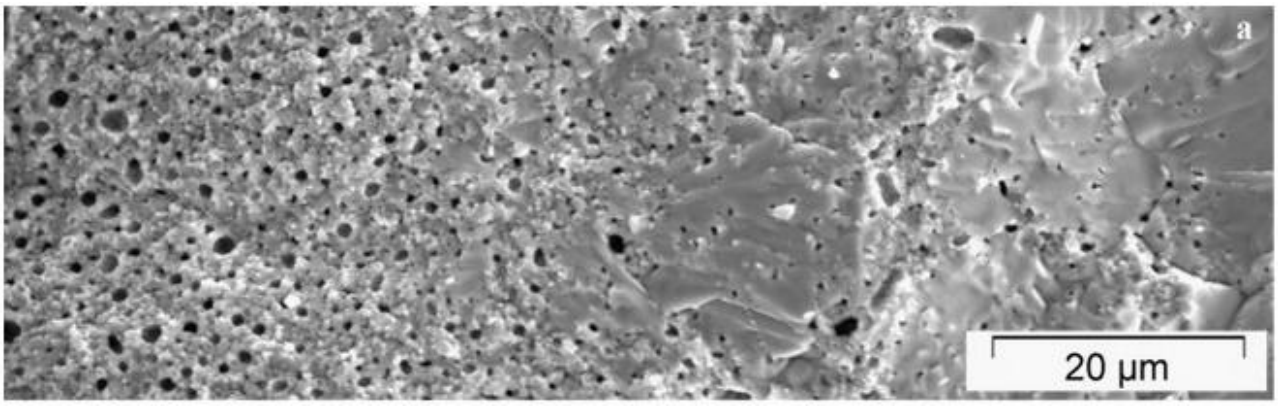

Figure 4 SEM image of the high burn-up structure in UO_2 near the rim region. Reprinted from Journal of Nuclear Materials, 372(2-3), J. Noirot, L. Desgranges, and J. Lamontagne, "Detailed characteristics of high burn-up structures in oxide fuels," 318-339, Copyright © 2008, with permission from Elsevier [17].

A significant amount of effort has been put into understanding grain growth behavior, which is an important type of microstructural evolution phenomena. During grain growth, the grain boundary mobility is usually described using the relation:

$$v = M \times F, \tag{1}$$

where v is the grain boundary velocity, M is the grain boundary mobility, and F is the driving force (in units of pressure) acting on the boundary. This is a first-order approximation based on the assumption that the driving force is significantly less than the thermal energy of the system ($F \ll k_B T$) [25]. Many different driving forces exist that can act on a grain boundary at any given moment in time (i.e. thermal gradient, magnetic, strain field, etc. [25, 26]), but one that is prevalent in polycrystalline systems is the curvature driving force. This driving force is described as the ratio of the stiffness of the grain boundary to the radius of the grain:

$$F = \Gamma / r_{grain}. \tag{2}$$

The stiffness of the grain boundary is the sum of the grain boundary energy and the second derivative of the grain boundary energy with respect to misorientation: $\Gamma = \gamma_{GB} + \gamma''_{GB}$. Determining the relationship between grain boundary energy and misorientation is a difficult task, and thus the second derivative term is often ignored under the assumption that it has no significant impact on the grain boundary mobility. Recent research has argued that the second derivative term is numerically significant however [27]. Equations (1) and (2) show that the grain boundary velocity is dependent on two grain boundary properties: the mobility (M), and the grain boundary energy (γ_{GB}). The anisotropy in these two properties is expected to play a significant role in grain boundary motion and microstructural evolution, thus making them important parameters to understand. Unfortunately, most mesoscale models (such as in phase-field modeling) assume an isotropic form, assigning a constant value to these properties for every boundary. While this provides a general way to examine grain growth, it is a well-established fact that anisotropy exists in these properties [25, 28-38]. Some works have examined prescribed forms of the anisotropy [39-41] and have discovered important trends regarding the relationship between the grain boundary character and anisotropy in these properties, but no experimentally based models have been developed.

To date, a significant amount of research has been performed to understand grain boundary migration and its mechanisms, although there are still many questions to be answered regarding these processes. Several different mechanisms have been identified, such as a coordinated shuffle (i.e. a martensitic transformation) [26, 32, 42], uncoordinated shuffle [42], rotational shuffle [41-43], and others [26, 44]. Despite the mechanisms identified, no clear method for determining which mechanism(s) will be active for any particular grain boundary has been developed. Additionally, for what would seem to be a thermally activated process, grain boundary migration only sometimes follows the typical Arrhenius behavior (i.e. a single, positive activation energy across all valid temperatures). For a property exhibiting Arrhenius behavior, the property (P) is defined by a pre-exponential coefficient (P_0) multiplied by an exponential with a specific activation energy (Q_0): $P = P_0 \exp\left(-Q_0 / k_B T\right)$. Many grain boundaries seem to have different mechanisms activated across different temperature ranges, leading to multiple activation energies that may not be indicative of the particular mechanism or set of mechanisms that move the boundary. Additionally, experiments [45, 46] and simulations [29, 32, 42, 47-50] have discovered boundaries that exhibit athermal (temperature-independent) or anti-thermal (rate decreases with increasing temperature) grain boundaries, distinctly at odds with Arrhenius kinetics, with no clear reason for why such behavior exists. The negative activation energies associated with the anti-thermal boundaries are meaningless [51], and indicative of a more general problem with how grain boundary migration is understood [49]. Some trends that have been identified for grain boundary migration are shown in Figure 5 (from Cantwell *et al*. [49]).

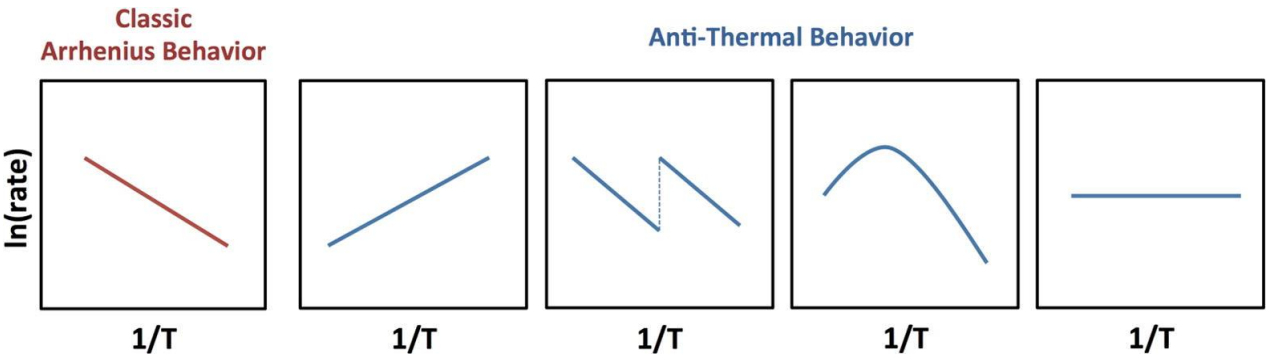

Figure 5 Different types of grain growth behavior as viewed in an Arrhenius plot. Reprinted from Scripta Materialia, 102, Patrick R. Cantwell, Elizabeth A. Holm, Martin P. Harmer, and Michael J. Hoffman, "Anti-thermal behavior of materials," 1-5, Copyright © 2015, with permission from Elsevier [49].

Another difficulty with understanding grain boundary migration is the parameter space associated with grain boundaries. A grain boundary has five macroscopic degrees of freedom [52]: three describe the misorientation between the two grains, and two describe the interface normal (called the inclination). The grain boundary character can be described as being either tilt, twist, or mixed (a combination of tilt and twist). Tilt grain boundaries have the boundary plane parallel to the rotation axis, while twist boundaries have the boundary plane perpendicular to the rotation axis (see Figure 6). Mixed boundaries have characteristics of both tilt and twist boundaries. Tilt boundaries can be further subdivided into symmetric and asymmetric tilt boundaries. In symmetric tilt boundaries, the boundary plane is a mirror plane, with atoms on one side of the boundary mirrored across the boundary plane. Asymmetric tilt boundaries are not mirrored across the boundary plane.

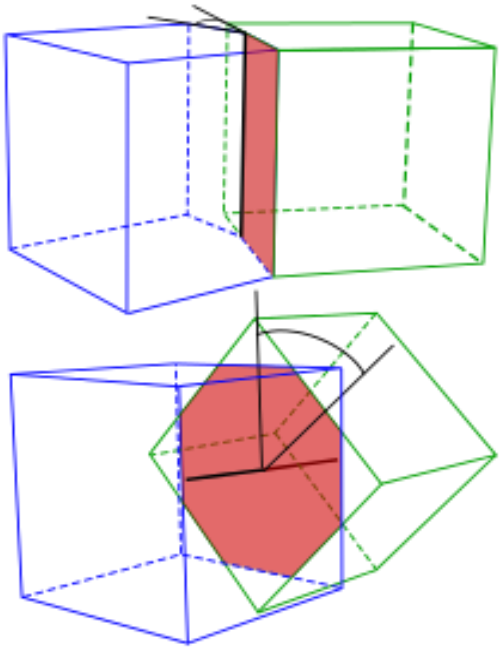

Figure 6 Schematic of tilt (top) and twist (bottom) grain boundaries. From Wikipedia user Slinky Puppet,

It is difficult to control each degree of freedom of a grain boundary in experiment. Certain manufacturing processes can lead to a dominant boundary type (i.e. deformation twinning), but experimental works in general are unable to create a specific boundary for study. Computational works have somewhat more control over the boundary being created, as a specific boundary can be identified and created for a particular study. However, due to the limitations of

current atomistic methods (e.g. molecular dynamics), such boundaries are often limited spatially to those with a relatively small periodic boundary unit cell, limiting the ability to describe any arbitrary boundary. Flat grain boundaries are commonly created to study a specific boundary behavior. A flat grain boundary can have each degree of freedom explicitly specified (provided that the periodic cell is not too large), making it ideal for understanding the attributes of a specific boundary. Curved grain boundaries are also commonly employed in grain growth simulations via quarter-loop [53], half-loop [30, 31, 36, 40, 41, 54], or cylindrical geometries [35, 55], as the curvature driving force is predominant for grain growth in polycrystals. The misorientation of the curved grain boundary is specified by determining an axis of rotation, and an angle of rotation. Due to the nature of a curved boundary, the inclination degrees of freedom are not uniquely specified, and instead are averaged across inclination-space (quarter-loop geometries average over a 90° angular range, half-loops over a 180° angular range, and cylindrical geometries over the full 360° angular range). Regardless of the driving force applied, it has been shown [56, 57] that, with proper attention to detail, different simulation methodologies will return similar mobility values for the same type of boundary.

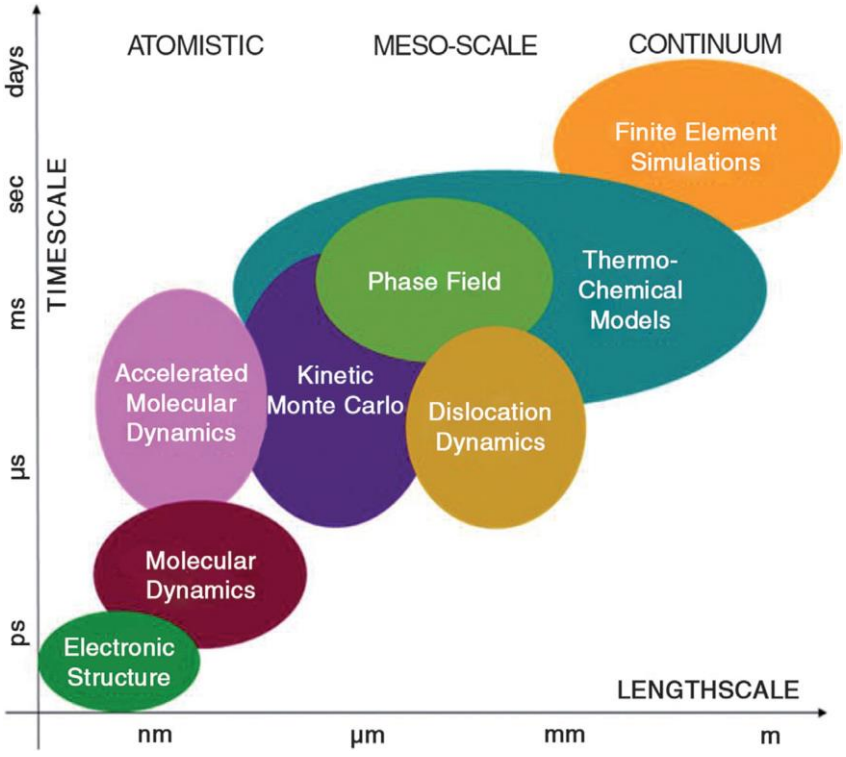

Figure 7 Time and length scales of various simulation methods (not comprehensive). Reprinted from Materials Today, 12(11), Marius Stan, "Discovery and design of nuclear fuels," 20-28, Copyright © 2009, with permission from Elsevier [58].

To model grain growth, different modeling methods operating at different time and length scales may be used, depending on the problem of interest. The common simulation methods for materials simulations are shown in Figure 7, although not all of them are suitable for grain growth. At the atomistic scale, one common approach is the use of molecular dynamics (MD) simulation to calculate grain boundary mobility. At the mesoscale, the phase-field method is typically used. MD uses a predefined interatomic potential (developed based on experimental and/or first principles simulation results) to describe atomic interactions, and covers lengths up to several tens of nanometers and times up to several nanoseconds. This limits the number of boundary types that can be studied. Coincident site lattice (CSL) boundaries have a specific unit cell that grows larger as the Σ number (which represents the inverse of the density of coincident lattice sites) increases. Because of the spatial limitations of these methods, only boundaries with relatively low Σ numbers can be simulated.

While much atomistic simulation work has been done over the past several decades to understand grain boundary mobility in materials, in particular in fcc metals, comparatively little has been done for oxide materials such as UO_2. Experimental works have examined grain growth in sintered UO_2 fuel pellets [59-61], but properties of individual grain boundaries have been sparse. Only one computational study (that the author is aware of) has been performed using UO_2 to study grain growth behavior of individual boundaries under a thermal gradient driving force [57]. Experimental studies done on fcc metals have indicated that <111> tilt boundaries generally move the fastest [48], and that <110> tilt boundaries move slower than both the <100> and <111> boundaries [62]. The anisotropy in mobility observed in experiments may be affected by the presence of impurities at grain boundaries [25]. Computer simulations can provide impurity-free grain boundaries so that the impurity effect can be removed. To date, no clear attempt has been made to identify the anisotropy of grain boundary mobility in UO_2, thus it is unclear what effect the presence of the oxygen sublattice will do to change the anisotropy. Thus, in this work, anisotropy in grain boundary energy and mobility in UO_2 will be studied. Both of these properties can be extracted from MD simulation. These properties may be used as inputs for mesoscale phase field simulations to better predict grain growth behavior in oxides.

Chapter 2 – METHODS

2.1 Molecular Dynamics Set Up

There are many different software options available for molecular dynamics simulation. In this work, the software of choice is the Large-scale Atomic/Molecular Massively Parallel Simulator (LAMMPS) developed and maintained by Sandia National Laboratory [63].

In all of the LAMMPS simulations in this work, the following commands were used:

- `units metal`: specifies that the values of the simulation will be given in metal units, namely energy in eV, distances in angstroms, time in picoseconds, etc. The LAMMPS manual contains the complete description of this unit style.
- `atom_style charge`: specifies that the system has charged atoms.
- `timestep 0.002`: specifies the time step used for all simulations is two femtoseconds.
- `dimension 3`: specifies the dimensionality of the simulation. All simulations in this work are performed in three dimensions.
- `boundary p p p`: specifies how the simulation deals with the box boundaries. `p` indicates that the boundary is periodic, meaning that the cell wraps around itself. One letter for each dimension is required.

The mass of each atom type was specified using the `mass` command, with the mass of uranium being 238.0289 g/mol, and the mass of oxygen being 15.9994 g/mol.

An important part of molecular dynamics simulation is the interatomic potential. Several potentials have been developed for UO_2, but this work will use the Basak potential [64] which is known to accurately predict elastic and defect data [65]. The Basak potential consists of a sum of three potential forms: a Coulomb potential (for charge interactions), a Buckingham potential (which consists of a term for core repulsion and a term for the van der Waals attraction), and a Morse potential (for anion-cation interactions). The final form of the potential is

$$U_{ij}(r_{ij}) = \frac{Aq_iq_j}{r_{ij}} + Be^{-r_{ij}/\rho} - \frac{C}{r_{ij}^6} + D_0[e^{-2\alpha(r_{ij}-r_0)} - 2e^{-\alpha(r_{ij}-r_0)}], \quad (3)$$

where B, ρ, C, D_0, α, and r_0 are fitting parameters, q_i and q_j are the charges for the atomic species (+2.4 for U and -1.2 for O), A is an energy conversion term, and i and j refer to the atomic species. Values for each fitted parameter are listed in Table 1. Note that the units given for parameters C and D_0 in the original paper [64] are incorrect, and should be J Å^6 and Å respectively (also note that the original paper has an additional factor f_0 (with units of Newtons) multiplied with D_0). We also note that the parameters determined by Govers *et al*. are slightly different from this work, due to converting kJ/mol to eV/molecule with a factor of 96.441 [66]. We use the factor of 96.485 to generate the parameters shown in Table 1.

Table 1 Fitted parameters for the Basak potential. Based on the values given in Govers et al. [65].

	U-U	O-O	U-O
B (eV)	294.640	1633.005	693.649
ρ (Å)	0.327022	0.327022	0.327022
C (eV Å^6)	0	3.949	0
D_0 (eV)	--	--	0.577188
α (Å^{-1})	--	--	1.65
r_0 (Å)	--	--	2.369

One difficulty with using the Coulomb potential with the Buckingham and Morse potentials is the difference between their effective interaction distances. The Coulomb potential is a long-range interaction, while the Buckingham and Morse potentials are short-range interactions. If the same cutoff values used for the short-range potentials were used with the long-range Coulomb potential, the calculated energies (and therefore mobilities) would be incorrect. However, specifying a large (global) cutoff value would be inefficient, as the short-range interactions would be at or near zero for a majority of the calculations. To address this, LAMMPS has implemented various algorithms that can calculate the Coulomb term in k-space

for interatomic distances beyond the (short-range) cutoff distance. The specific algorithm used in this work is the particle-particle particle-mesh method [67], with a desired accuracy of $1.0e-5$ (`kspace_style pppm 1.0e-5`).

To implement the Basak potential in LAMMPS, the `hybrid/overlay` pair style with the Buckingham and long-range Coulomb force combined with the Morse potential was used. This command takes the form: `pair_style hybrid/overlay buck/coul/long <cutoff1> morse <cutoff2>`. The cutoff used for both potentials was 11.0 angstroms. The pair coefficients were then specified using the `pair_coeff` command as follows:

`pair_coeff 1 1 buck/coul/long` B^{U-U} ρ^{U-U} C^{U-U} 11.0

`pair_coeff 1 2 buck/coul/long` B^{U-O} ρ^{U-O} C^{U-O} 11.0

`pair_coeff 2 2 buck/coul/long` B^{O-O} ρ^{O-O} C^{O-O} 11.0

`pair_coeff 1 2 morse` D_0^{U-O} α^{U-O} r_0^{U-O} 11.0

where the `1` refers to U atoms, the `2` refers O atoms, and the specific parameters are taken from Table 1. The `buck/coul/long` command automatically takes care of the *A* term in the Coulomb interaction.

LAMMPS can output some thermodynamic data (such as temperature, pressure, volume, etc.), as well as individual atomic information. 'Snapshots' of the structure at any given time step can be placed in 'dump' files, which can contain various user-specified atomic properties, including positional coordinates, velocities, and other per-atom properties. The thermodynamic data output is determined via the `thermo_style` and `thermo` commands, while the individual atomic data output is determined by the `dump` command. For all simulations in this work, the thermodynamic output contained at least the temperature, pressure, and potential energy, and the dump files contained the atom positions, type, and charge for each snapshot.

2.2 Evaluation of Interatomic Potential

Results from a molecular dynamics simulation are only as good as the potential being used to describe the atomic interactions. It is thus important to test the usage of the potential to make sure that the results gathered fit in well with other published values. In this work, three

evaluation calculations were performed: the cohesive energy of a UO_2 molecule, the lattice expansion with temperature, and the approximate melting temperature.

2.2.1 Cohesive energy

The cohesive energy of a system is defined as the amount of energy each individual atom (or molecule) has when located in its ideal position. To calculate this, a small single crystal of UO_2 was created, consisting of ten unit cells in each direction. LAMMPS has implemented algorithms to generate any arbitrary lattice structure with an arbitrary number of basis atoms. For UO_2, the 0 K lattice parameter is 5.453Å (as predicted by the Basak potential [65]), so the U atoms were generated using the `lattice fcc 5.453` command. The oxygen atoms are located at the tetrahedral sites in the fcc lattice, and had to be specified explicitly. This was done using the `lattice custom` command, and for one O atom, looks like `lattice custom 5.453 basis 0.25 0.25 0.25`. The other tetrahedral atoms were generated in the same command by adding additional `basis` keywords with the appropriate fractional coordinates. Once the structure was created, a conjugate-gradient minimization was performed to minimize the system energy. LAMMPS outputs the final energy after the minimization. The cohesive energy of a UO_2 molecule is then that system energy divided by the number of UO_2 molecules in the system (or, equivalently, the number of U atoms).

2.2.2 Thermal lattice expansion

Most materials will expand when exposed to increasing temperatures. To determine the amount of lattice expansion experienced as a function of temperature, a series of short simulations using a 10x10x10 cell were performed at temperatures ranging from 50 K to 3300 K, using the isobaric-isothermal ensemble. For each temperature, a series of ten simulations was performed to calculate an average lattice parameter. The simulation box lengths in each direction were included as part of the thermodynamic output. After allowing the system to equilibrate, the box lengths in each direction were averaged over the remainder of the simulation run. A Piecewise function consisting of a linear fit and a parabolic fit was fitted to the averaged data to create a function describing the lattice parameter as a function of temperature. The fit was performed using the Piecewise Fit app in Origin®. This fit was used because of the

apparent linear increase in lattice parameter as a function of temperature in a low-temperature range, with a transition to parabolic increase in a high-temperature range.

2.2.3 Basak melting temperature

Knowing the melting temperature of the interatomic potential being used is important to understand how well the simulated behaviors match with experiment. For UO_2, the experimental value of the melting temperature is around 3120 K [68]. Govers *et al*. [69] set up a simulation system of two blocks: one was a solid single crystal of UO_2, and the other was a 'block' of liquefied UO_2 (obtained from simulating the material at a very high temperature). Using this method, they determined that the Basak potential predicts a melting temperature around 3540 K. This work follows the same idea to determine the melting temperature. Two 10x10x10 structures were generated. For the first structure, a simulation run at 5000 K was performed to generate a melted UO_2 system, which was subsequently cooled to 3700 K. The second structure was run at 3400 K to generate a solid structure at high temperature. The melting temperature is defined as the temperature at which the solid and liquid phases of the material coexist. Thus, the solid and liquid structures were concatenated along the *x* direction, being careful to not overlap atoms. This combined structure was run for two nanoseconds using the micro-canonical ensemble (NVE). When the structure maintained a liquid and a solid phase in coexistence, the resulting temperature was used as the melting temperature.

2.3 Grain Boundary Structure

The grain boundaries used in this work are cylindrical grain boundaries. These boundaries were created by first creating a thin plate of a single crystal of UO_2 using GBStudio [70, 71], an example of which is shown in Figure 8. The *z*-axis of the plate was aligned with the desired rotation axis, being either [001] for <100> boundaries, [110] for <110> boundaries, or [111] for <111> boundaries. The orientations of each axis with the associated number of unit cells in each direction and the total number of atoms are shown in Table 2. This single crystal was used as input to create a series of grain boundaries. A grain boundary was created by rotating atoms within a radius, r_{grain}, from the center of this structure by a desired misorientation angle, θ (see Figure 9). The fluorite crystal structure has a four-fold rotational axis about <100>, a two-fold rotational axis about <110>, and a three-fold rotational axis about <111>. Because of

these symmetries, grain boundaries were created in a subset of the 360° misorientation range: 0° − 90° for <100>, 0° − 180° for <110>, and 0° − 120° for <111>. Grain boundaries were created with misorientations in increments of 5°, with additional angles associated with low Σ numbers in each rotation axis (i.e. Σ5 (310) is a <100> boundary with a misorientation angle of 36.87°). This was done to increase the detail of the profile, and examine common CSL boundary misorientation angles.

Generating the grain boundary structure in this way often leaves atoms overlapping at the boundary. Starting a MD simulation under such conditions would generate unrealistically high energies, which would rapidly increase the system energy, destabilizing the structure. To address this issue, two cutoff radii were used to determine what atoms should be removed: r_{cut}^{U-U} = 2.5 Å and r_{cut}^{O-O} = 0.64 Å. If a pair of same-element atoms were closer than the respective cutoff radius, one of the pair of atoms was removed. Charge neutrality of the system was maintained by removing atoms at a ratio of one uranium atom for every two oxygen atoms. To determine which atoms were removed, first a neighbor list was generated for each atom. For each atom specified to be removed, the neighbor list would be searched to find the two closest atoms to maintain the 1U:2O ratio, and mark them for removal as well (i.e. if an oxygen atom was marked for removal, the closest U and O atoms in its neighbor list would also be marked for removal). Note that removing atoms in this way can generate local charge imbalances, which could affect the overall behavior of the system.

Table 2 Single crystal setup for the three rotation axes examined in this work. Length is given in angstroms.

	<100>			<110>			<111>		
	Direction	Number of Cells	Total Length	Direction	Number of Cells	Total Length	Direction	Number of Cells	Total Length
x	[100]	50	272.6	[001]	43	234.4	$[1\bar{1}0]$	35	269.9
y	[010]	50	272.6	$[1\bar{1}0]$	29	223.6	$[11\bar{2}]$	20	267.1
z	[001]	5	27.26	[110]	5	38.55	[111]	3	28.33
N	150000			149640			151200		

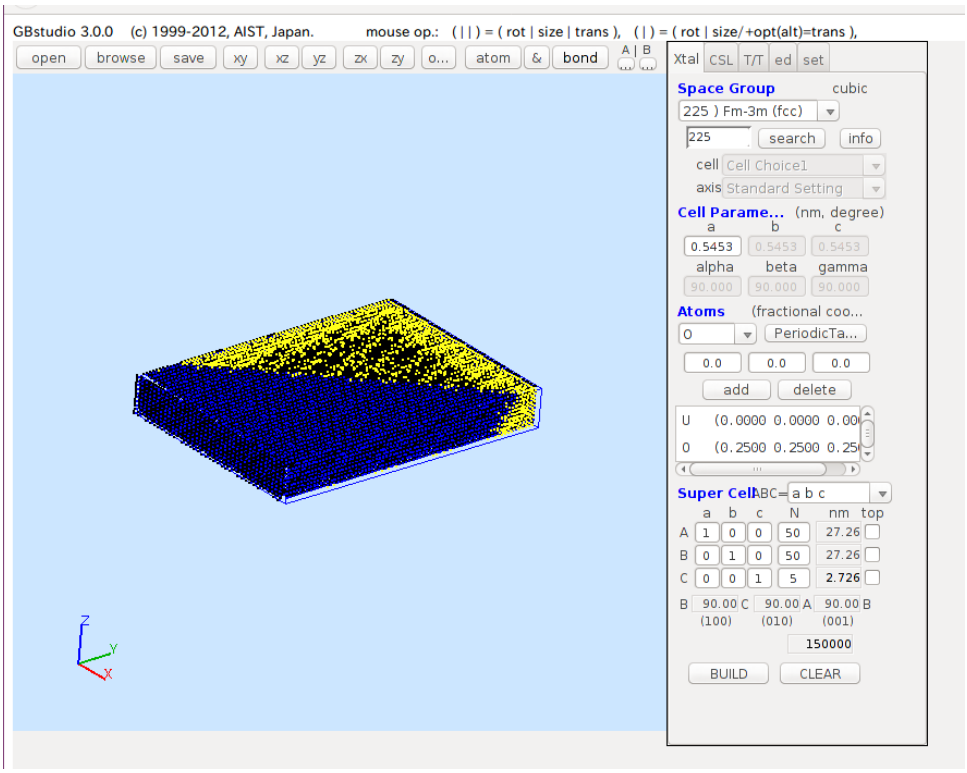

Figure 8 Example of GBStudio crystal creation. This particular example creates a crystal oriented along <100>.

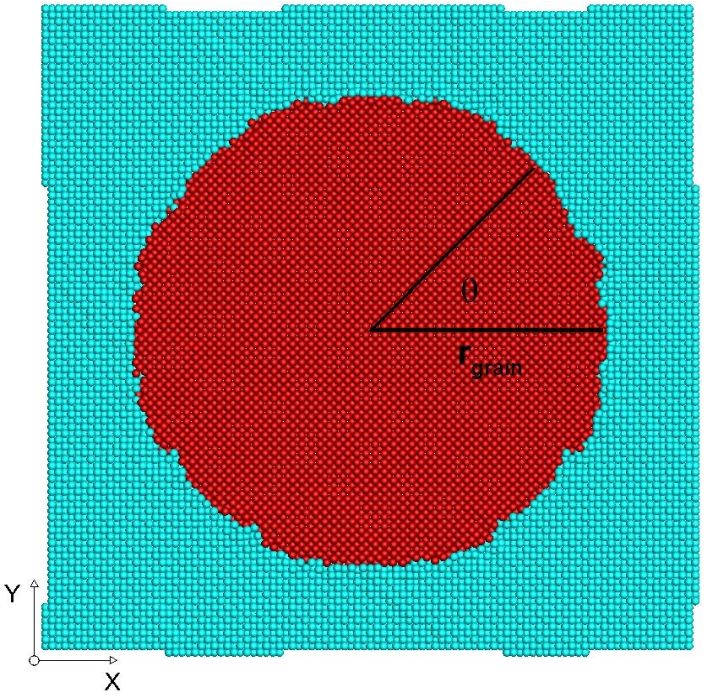

Figure 9 Creation of the cylindrical grain boundary. Atoms within a distance r_{grain} from the center of the structure were rotated by the desired misorientation angle θ.

2.4 Grain Boundary Energy Calculations

The grain boundary energy calculations were performed using a three-step process to generate a minimum energy configuration. The first step was a conjugate-gradient-based energy minimization at 0 K. LAMMPS has implemented the Polak-Ribiere version [72] of this algorithm. The second step was a thermal annealing at 1500 K. A short simulation (100 picoseconds) was then run, using the canonical (NVT) ensemble. This ensemble maintains a constant number of atoms (N), a constant volume (V), and a constant temperature (T). The volume was kept constant during this process to prevent lattice expansion due to the thermal energy. LAMMPS has implemented the Nosé-Hoover equations of motion [73-75], which allows the system temperature to be constrained. Performing this step potentially allows the atoms to move out of a shallow potential energy well, giving them the chance to move to a deeper well. After this annealing step, a second conjugate-gradient minimization was performed at 0 K. Snapshots of the simulation were saved before and after each conjugate-gradient minimization and every 20 picoseconds during the annealing process for analysis.

A visual analysis of the grain boundary structure was performed after running the LAMMPS simulations. These analyses were performed using OVITO [76]. In these analyses, the size of the cylindrical grain was inspected to make sure that the structure did not experience significant growth. If there was a significant difference in grain size between the snapshot after the first and second conjugate-gradient minimizations, the energy values from the first minimization were used. If no significant growth was observed, then the system energy from the second minimization was used.

Grain boundary energies were calculated by comparing the system energy of the grain boundary structure to the system energy of the single-crystal plate:

$$\gamma_{GB} = \frac{U_{GB} - \frac{N_{GB}}{N_0} U_0}{2\pi r_{grain} L_z} \tag{4}$$

where γ_{GB} is the grain boundary energy, U_{GB} is the system potential energy of the grain boundary structure, U_0 is the system potential energy of the single crystal, N_{GB} and N_0 are the

number of atoms for the grain boundary structure and single crystal structure respectively, and L_z is the thickness of the plate (height of the cylinder). In all grain boundary energy calculations, r_{grain} = 100 Å.

2.5 Grain Boundary Mobility Calculations

Grain boundary migration is a thermally activated process that is generally assumed to follow Arrhenius kinetics. Thus, to calculate the activation energy and prefactor of the mobility of a grain boundary, multiple simulations needed to be run at different temperatures. The temperatures tested ranged from 1700 K to 3300 K, and up to five simulations were performed to improve the statistics for each temperature examined. The statistical ensemble used for the mobility simulations was the isothermal-isobaric ensemble (NPT). The reason for using this ensemble was to allow the system to expand based on the temperature. LAMMPS has implemented a Nosé-Hoover barostat as well, allowing the pressure to be maintained at a constant value. For these simulations, the pressure was maintained at zero bars independently in each direction. To get accurate data, simulations were run from 1.6 nanoseconds in the shortest simulations, to ten nanoseconds in the longest simulations. Simulations in general ran until the grain completely shrank, but this became impractical at lower temperatures.

The input structure for the mobility simulations was the final structure after the above minimization process for grain boundary energy. Grain boundary mobilities were determined for six specific boundaries: a 45° and 20° misorientation for each of the <100>, <110>, and <111> rotation axes. In order to calculate the grain boundary mobility, a relationship between the mobility and a tracked parameter was needed. The velocity of the grain boundary in these simulations is $v = dr_{grain} / dt$. Due to not being able to explicitly calculate the grain boundary stiffness, the simplified form of the driving force was used: $F = \gamma_{GB} / r_{grain}$. Combining these relationships into Equation (1):

$$\frac{dr_{grain}}{dt} = M \frac{\gamma_{GB}}{r_{grain}}. \tag{5}$$

By combining like terms and integrating (dropping the subscript on r_{grain}):

$$\frac{1}{2}\frac{dr^2}{dt} = M\gamma_{GB}. \tag{6}$$

Multiplying both sides by π creates the term πr^2, the area of a circle. In the context of the cylindrical grain boundary, this is the cross-sectional area of the cylindrical grain. This can then be written as:

$$\frac{1}{2\pi\gamma_{GB}}\frac{dA}{dt} = M, \tag{7}$$

where A is the cross-sectional area of the cylindrical grain at any given time. The orientation parameter method [31, 57] was used to determine A. This method assigns each atom a value based on the orientation of the atoms around it via:

$$f_i = \frac{1}{n}\sum_{j=1}^{n}\left(3-2\cos^2\theta_{ij}\right)^2\cos^2\theta_{ij}. \tag{8}$$

Here, n is the number of nearest neighbor atoms within a specified cutoff radius from atom i, and θ_{ij} is the angle between the vector connecting atoms i and j and the reference vector in the [100] direction of the matrix grain. For atoms in the bulk of either grain, far from the grain boundary, a single value will be given. Different orientations will give different values, allowing for differentiating between the two grains. As atoms at the boundary typically will not have either of the two values, a cutoff value was used to assign boundary atoms to a grain. This value varied depending on the orientation axis examined. Using this method, the number of atoms, N in the cylindrical grain can be determined. This value can then be used to determine the volume of the cylindrical grain based on the relationship $V = N(a_0(T))^3/4$, where $a_0(T)$ represents the temperature-dependent lattice parameter of a single UO_2 crystal. As grain boundary migration is limited by the slowest moving species, only the uranium atoms (located at fcc sites in the structure) were tracked and used in these calculations. The cross-sectional area of the grain is simply the volume of the cylinder divided by the cylinder height (L_z): $A = N(a_0(T))^3/4L_z$.

The orientation parameter in a perfect fcc lattice (i.e. the U sublattice) when oriented along <100> would have a maximum value of 1.5, and a minimum value of 1.0 (corresponding to misorientations of 45° and 0° respectively). This value is based on the first nearest uranium neighbors. During simulations, thermal vibrations can cause this number to fluctuate, sometimes

significantly from the expected value. This issue was addressed by specifying a cutoff value to determine which atoms to include in the orientation parameter calculations. This work used a cutoff value halfway between the ideal first nearest neighbor and second nearest neighbor distances ($r_{cut} = 0.854a_0$).

The average grain growth behavior was calculated by averaging the grain area across all simulations at each time step (i.e. if there were three simulations run for T = 3000 K, the areas at time step 0 would be averaged, then the areas at time step 10,000 would be averaged, then 20,000, etc.). Once the averaged area as a function of time was known for each temperature, a linear fit was performed to the range of data where grain growth occurred. This fit was performed using Gnuplot. User interaction dictated where the growth started and stopped to allow for excluding initial and final transients in the grain growth behavior.

2.6 Grain Rotation Analysis

Normal grain growth can be accompanied by a shear acting parallel to the grain boundary plane. In a cylindrical grain boundary, this manifests by rotating the cylindrical grain. Quantitative determination of the grain rotation angle is beyond the scope of this work. However, a qualitative look at the rotation experienced by the shrinking grain is possible. After a simulation was complete, the first dump file (containing the initial structure) was marked with a strip down the center of the structure. This strip was initially parallel to the y-axis, and covered approximately one tenth of the distance in the *x* direction (see Figure 10). The atoms that were in this strip had their IDs taken. Two more dump files were analyzed: the dump file where the grain had shrunk by approximately half (or, in the case of incomplete grain growth, the halfway point of the simulation), and the final dump file for complete shrinkage (in most cases). The same atoms (based on ID) were compared in these dump files. If the grain experienced any rotation, the initially straight line would have an s-shaped curve by the final snapshot. Grain rotation was qualitatively assessed in this way.

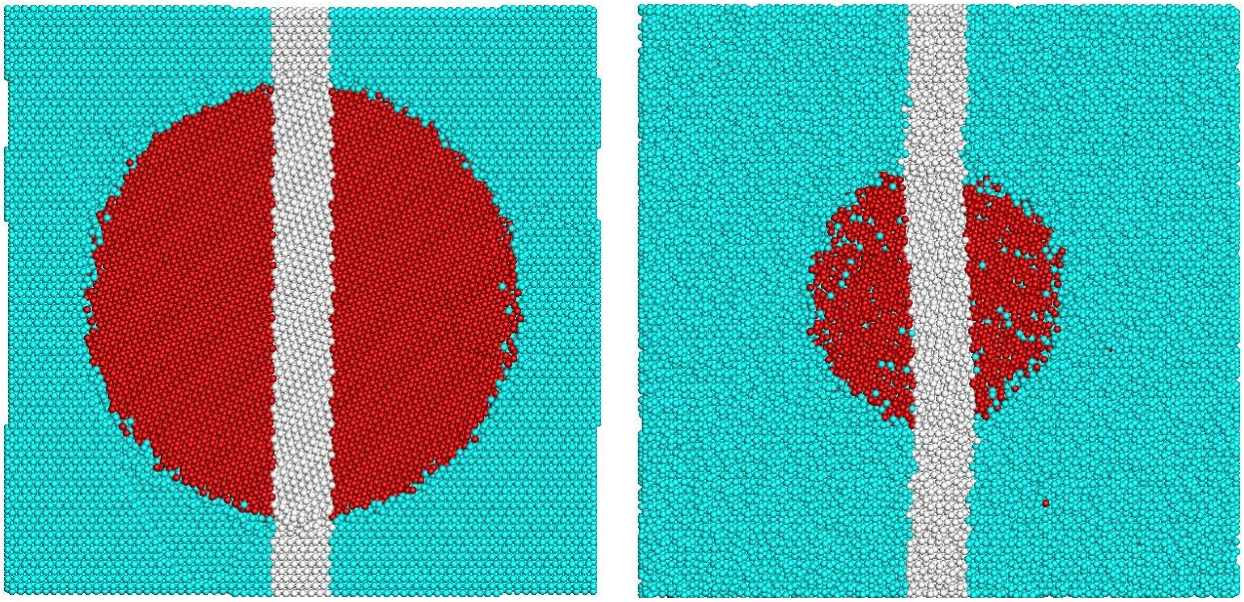

Figure 10 Example of the strip used to qualitatively track grain rotation during grain growth. Atoms in the center strip had their IDs taken, and the same IDs were examined in subsequent snapshots. As the simulation continues, any rotation of the cylindrical grain will manifest as a deviation from a straight line.

Chapter 3 – RESULTS AND DISCUSSION

3.1 Basak Potential Evaluation

Table 3 and Figure 11 show the comparisons of the cohesive energy, melting temperature, and thermal lattice expansion with published works. The percent error for the cohesive energy is less than 0.1%, indicative of a correct use of the potential. The difference in the temperature-dependent lattice constant between this work and Basak *et al*. [64] is also negligible, as shown in Figure 11. The melting temperature is about 100 K lower than the value determined by Govers *et al*. [69]. The calculated fit for the lattice parameter as a function of temperature takes the form:

$$a_0(T) = \begin{cases} aT + b & 0 \le T \le T_c \\ cT^2 + dT + e & T_c < T \le 3300 \end{cases} \tag{9}$$

where the coefficients *a, b, c, d, e,* and T_c are shown (with fitting errors) in Table 4.

Table 3 Comparison of calculated values of cohesive energy and melting temperature with published works.

Parameter	This work	Published work	Percent Error
Cohesive energy (eV)	–43.235	–43.2 [65]	0.08%
Melting temperature (T)	3440 ± 25	3540 ± 65 [69]	2.82%

Table 4 Fitted parameters and fitting errors of the lattice parameter as a function of temperature.

	a (Å / K)	b (Å)	c (Å / K^2)	d (Å / K)	e (Å)	T_c (K)
Fitted value	5.94×10^{-5}	5.4531	4.9×10^{-9}	6.4×10^{-5}	5.442	1110
Fitting error	6.0×10^{-7}	4.0×10^{-4}	4.0×10^{-10}	2.0×10^{-6}	2.0×10^{-3}	40

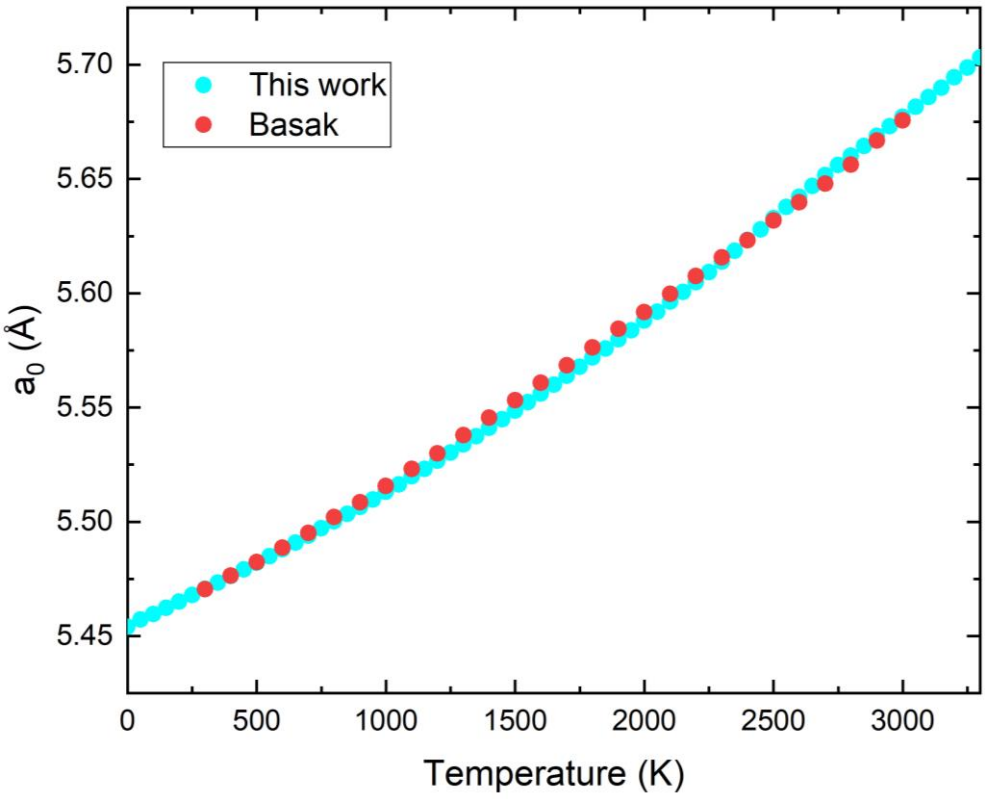

Figure 11 UO_2 lattice parameter as a function of temperature as calculated in this work, compared with the results from Basak *et al*. [64]. Data points from Basak *et al*. extracted using WebPlotDigitizer.

3.2 Grain Boundary Energy

The results for the grain boundary energy as a function of misorientation angle for the <100>, <110>, and <111> rotation axes are shown in Figure 12. Across all boundaries examined, the highest grain boundary energy was near 2.0 J/m^2, and the lowest was near 1.25 J/m^2. Across the high-angle misorientation range ($>15°$), the lowest value was approximately 1.5 J/m^2. This relatively small range of values seems to indicate that anisotropy in grain boundary energy is insignificant. In addition, no large cusps are observed, which is different from the grain boundary energies in pure metals [77]. Additional grain boundary energy calculations were performed for a low-symmetry rotation axis, <112>. Those results (shown in Figure 13) also demonstrate a fluctuation around 1.7 J/m^2, similar to the three high-symmetry rotation axes. Future work can identify if other low-symmetry boundaries have more fluctuation in grain boundary energy, or if there are specific rotation axes that have unique features not shown in the few rotation axes examined. Bai *et al*. [57] calculated grain boundary energies for five different special grain boundaries (i.e., CSL grain boundaries) consisting of symmetric tilt or

twist character, and found a grain boundary energy varying between 1.02 J/m^2 and 1.61 J/m^2. The average value of grain boundary energy from that work is approximately 1.55 J/m^2, which is slightly lower than the values obtained from this work using inclination-averaged cylindrical grain boundaries. In the grain boundary mobility calculations of this work, a single grain boundary energy value of 1.6 J/m^2 was assumed (the approximate midpoint between the results of Bai *et al*. and this work). Because of the relative lack of the typical "cusp" features in the grain boundary energy profile for the boundaries examined, the anisotropy in grain boundary energy is assumed to have an insignificant effect on the grain growth behavior.

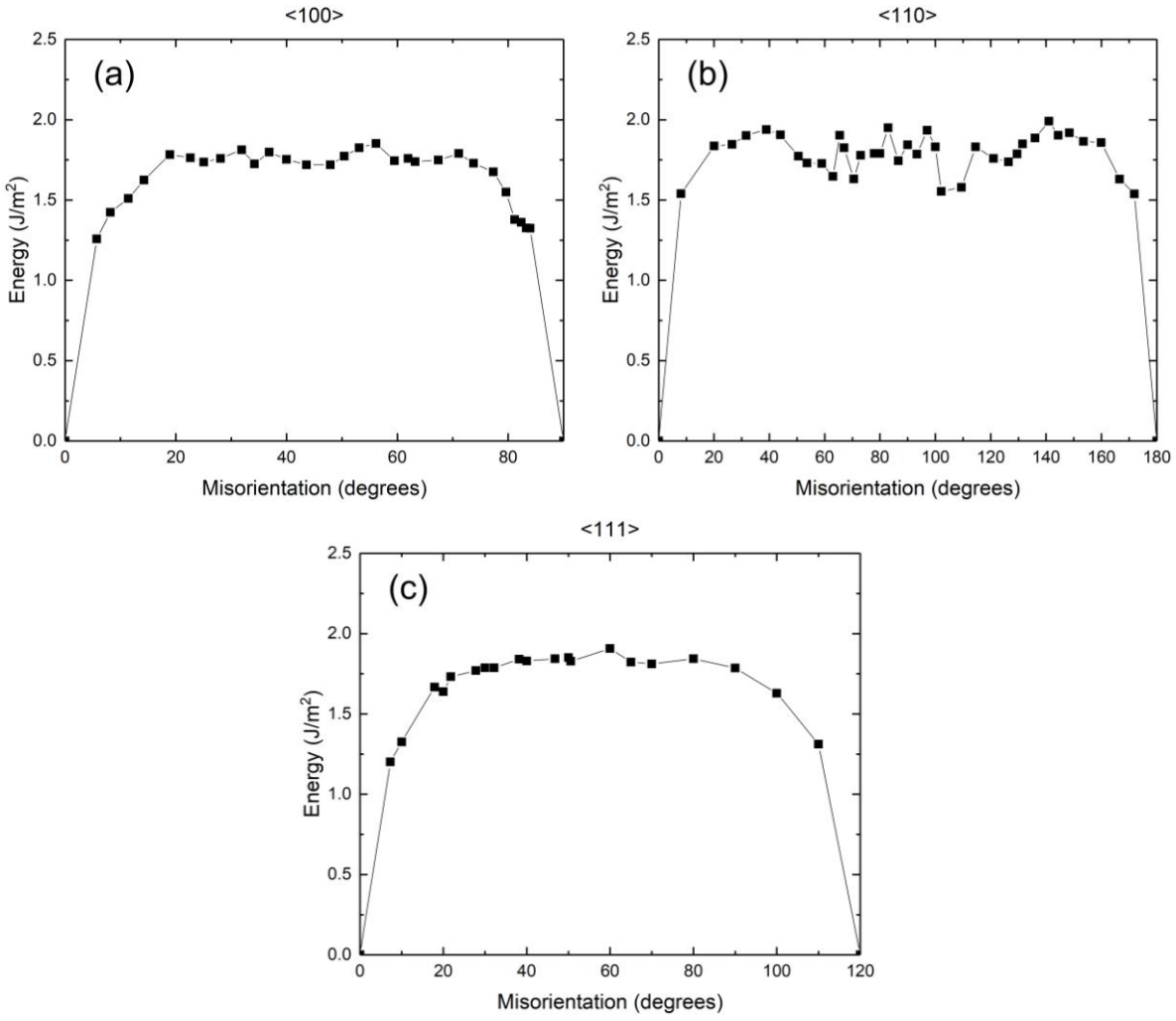

Figure 12 Grain boundary energies for the three rotation axes examined. (a) <100>, (b) <110>, and (c) <111>. The lines are guides for the eye.

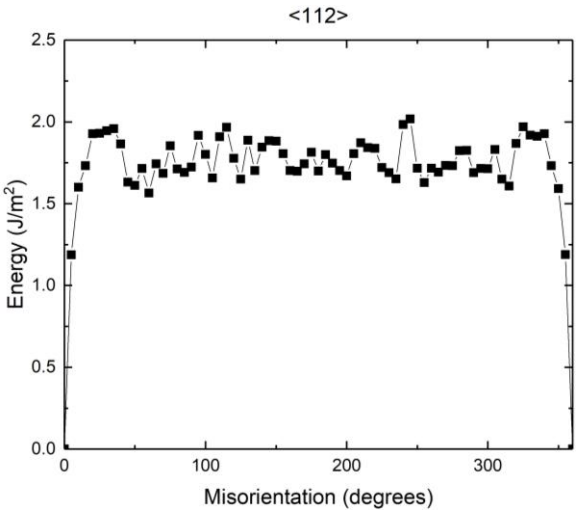

Figure 13 Grain boundary energy for the low-symmetry rotation axis <112>.

Olmsted *et al*. [28] predicted that a proper interpolation scheme would be able to determine grain boundary energies for any Cu, Ni, Al, and Au boundary in the five-space based on just their 388 grain boundary energy database. Bulatov *et al*. [77] was able to develop such an interpolation scheme for these four fcc metals by successive fitting from low- to high-dimensional data (i.e. starting with a one-dimensional fit to specific subsets in the five-space, then using those fits to interpolate a two-dimensional fit, etc.). Their results show that such an interpolation scheme works, if the input parameters are correctly tuned. Because of the similarities between the fluorite structure and the fcc structure, it is expected that a similar fit would work for UO_2. Undergraduate interns at INL have worked on this, and have found similarities (as expected) [78-83]. However, additional information is needed to determine the parameters necessary for grain boundary energy interpolation. The <112> tilt UO_2 grain boundary energies shown in Figure 13 are compared with the five-degree-of-freedom (5DoF) model for UO_2 developed at INL (Figure 14a). The 5DoF model has large discrepancies with the MD results obtained from this work, suggesting that the model may not work well for low-symmetry axes. It should be noted that Bulatov *et al*.'s 5DoF model works very well for <112> boundaries in Al (Figure 14b) and Cu (Figure 14c), in which the grain boundary energies are calculated using cylindrical grain boundaries. Clearly, the 5DoF model for the fcc metals works very well, while for UO_2 it does not. Therefore, the grain boundary energies calculated from this work can provide additional fitting data for improving the existing 5DoF model for UO_2 that is being developed at INL.

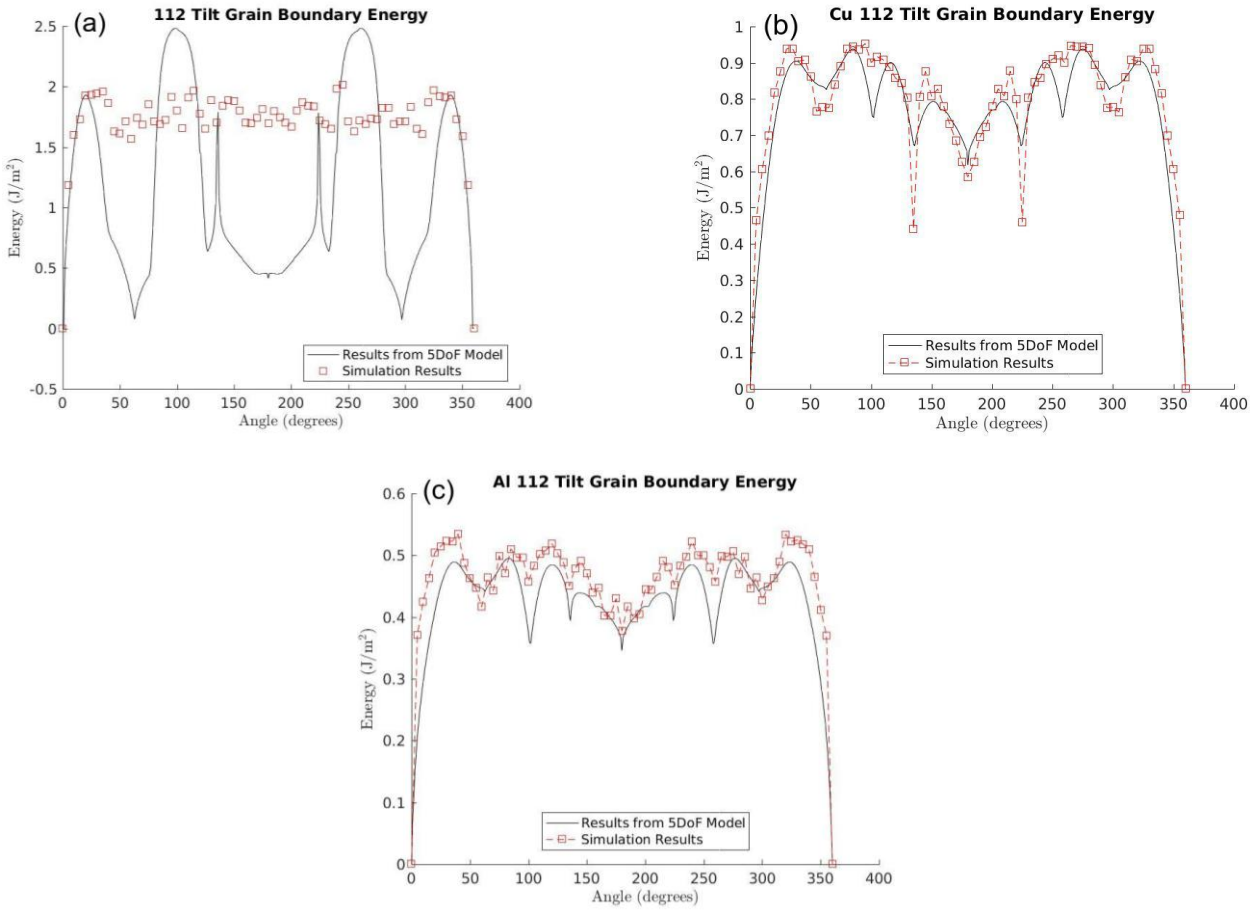

Figure 14 Grain boundary energy simulation results compared with predicted results for the low-symmetry <112> rotation axis using the Bulatov (5DoF) model [77]. (a) UO_2, (b) Cu, (c) Al.

3.3 Grain Boundary Mobility

Grain boundary mobility results will proceed as follows. First, evidence of grain growth is presented for the boundaries studied in Section 3.3.1. Then, the finite size effect is examined in Section 3.3.2. Two aspects of anisotropy are then examined: misorientation anisotropy in Section 3.3.3, and rotation axis anisotropy in Section 3.3.4. Finally, grain rotation is presented and discussed in Section 3.3.5.

3.3.1 Evidence of grain growth

The first step in determining grain boundary mobility is verifying that grain growth is occurring at the temperatures being examined. Snapshots of the <100> 45°, <110> 45°, and <111> 45° boundaries with T = 3000 K at the beginning, middle, and end of the simulations are shown in Figure 15. The initial radius for all three of these boundaries is 100 Å. This series of

images shows that grain growth is occurring in the boundaries examined at this temperature. Additionally, the rate of growth is different between the different rotation axes, as indicated by the simulation times for each image. The <111> boundary appears to migrate the fastest, while the <110> boundary migrates the slowest. This behavior is shown more clearly in Figure 16, where the area of the shrinking grain as a function of time is shown for the same three boundaries. This plot also demonstrates the linearity of the rate of grain shrinkage at this temperature, justifying the use of a linear fit to the area as a function of time.

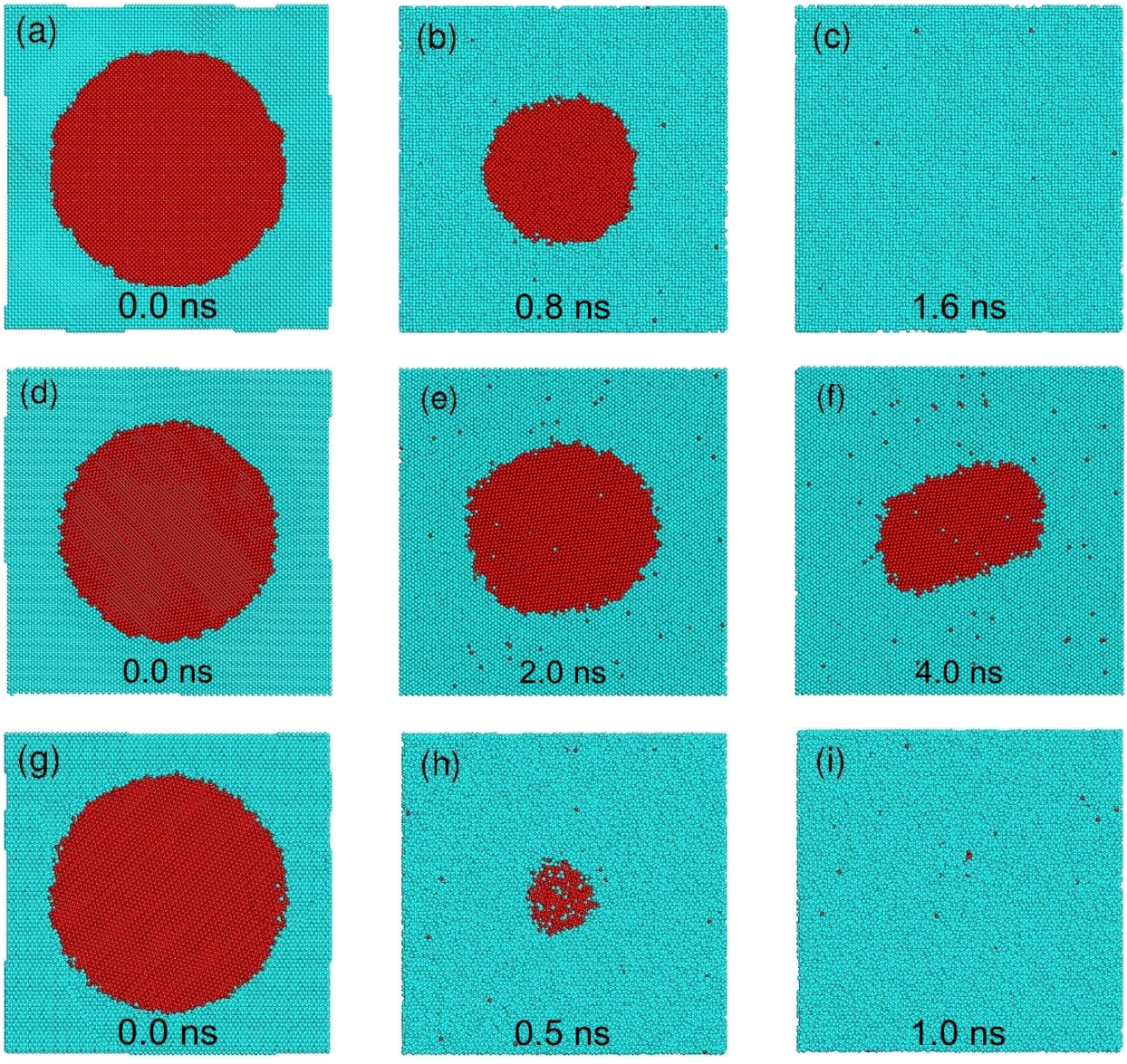

Figure 15 (a-c) <100>, (d-f) <110>, and (g-i) <111> 45° boundary snapshots at the beginning (first column), middle (second column), and end (last column) of simulations with a temperature of 3000 K, demonstrating various grain growth rates.

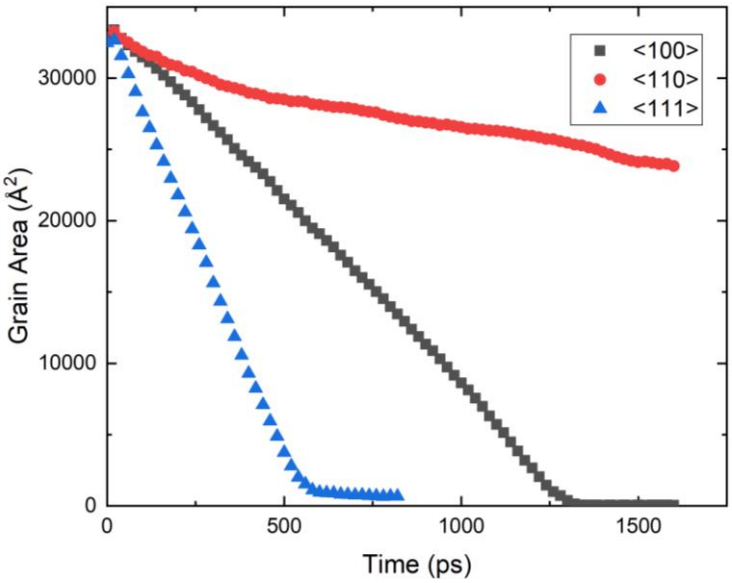

Figure 16 Area of the cylindrical grain as a function of time for the <100>, <110>, and <111> 45° boundaries. The slope of each curve is proportional to the boundary mobility

To verify the existence of grain growth at a range of temperatures, a similar analysis was performed for T = 2500 K and T = 3300 K. Figures 17 – 19 show the area versus time plot for the <100>, <110>, and <111> axes respectively for these temperatures, along with the data at T = 3000 K (from Figure 16). These figures show that grain growth is dependent on temperature. Additionally, it is seen that the linear fit works well across a range of temperatures and misorientations. However, as the temperature decreases for the <100> boundary, it appears that the area versus time is better described by a parabola. The presence of curvature at these lower temperatures could be indicative of at least two things. One, the mobility of the boundary in question may not follow simple Arrhenius kinetics, and the curvature may represent a change in the weighted averages of the different mobilities. Two, the mobility of the boundary could be curvature dependent. If a parabolic fit to the lower-temperature data was performed, the implicit assumption in doing so is that the mobility is linearly dependent on time and thus the grain radius (as opposed to a constant). Either of these explanations will require further study. In this work, a linear relationship between the driving force and the grain boundary velocity was assumed by linearly fitting to a subset of the data.

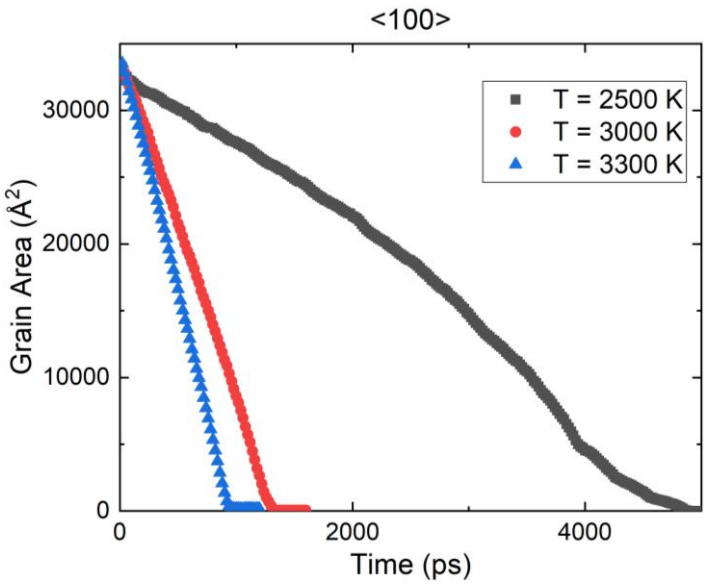

Figure 17 Area as a function of time for the <100> 45° boundary at three temperatures. Note that at the lower temperature the area versus time plot deviates from the linear decrease behavior.

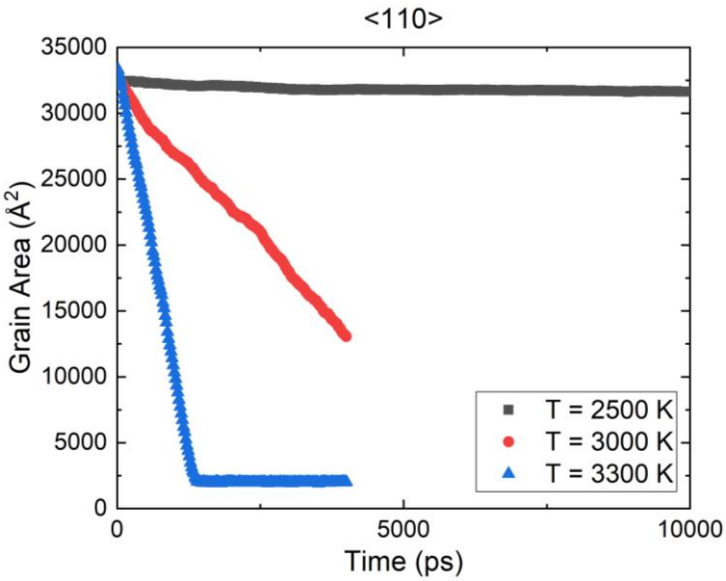

Figure 18 Area as a function of time for the <110> 45° boundary at three temperatures. At the lowest temperature shown, no significant growth was experienced in the first ten nanoseconds.

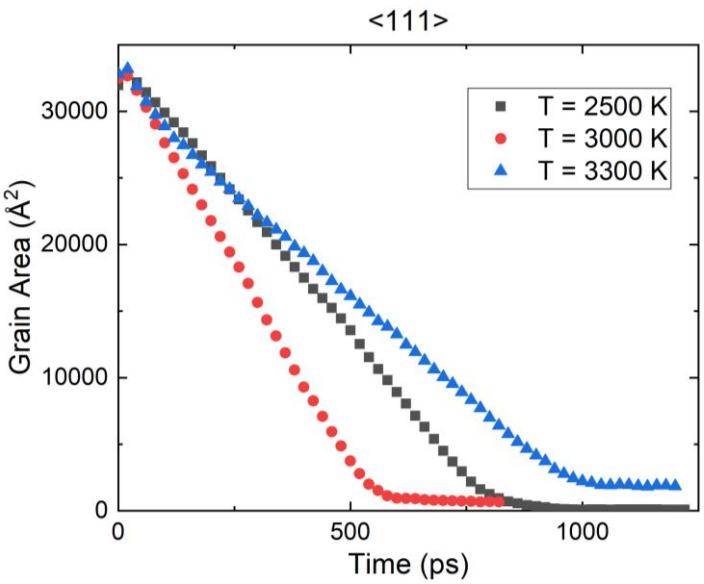

Figure 19 Area as a function of time for the <111> 45° boundary. Unique to this boundary is the apparent slow down at higher temperatures, as the highest temperature shown appears to migrate more slowly than the lowest temperature.

3.3.2 Finite size effect

At small length scales, the system and grain sizes can have an impact on the overall behavior. The finite size effect was examined by a) varying the initial grain radius (while keeping the same system size), and b) increasing the system size (while maintaining the same grain size).

3.3.2.1 Initial grain radius

As the temperature decreases, the rate of grain growth tends to decrease as well (as shown in Figures 17 – 19). Recalling that the definition of the curvature driving force is the ratio of the grain boundary energy to the radius of the grain (see Equation (2)), the driving force can be increased either by increasing the energy of the boundary, or by decreasing the radius of the grain. Since the anisotropy in grain boundary energy is small, the grain growth rate will not be increased significantly by increasing the grain boundary energy. Here, to achieve significant grain growth at low temperatures, the initial grain radius can be decreased. Two grain radii were

examined: r_{grain} = 100Å and 75Å. Figure 20 shows the Arrhenius plot of the calculated mobilities for the <100> 45° boundary using these two initial grain radii. The r_0 = 100 Å data shows a single linear trend at T > 2300 K. In the same temperature range, the r_0 = 75 Å data also shows a single linear trend. Using the two different initial radii, the mobilities are similar, although the smaller radius gives slightly higher mobilities. However, as the temperature continues to decrease (beyond the range where the r_0 = 100 Å grain could experience significant grain growth in MD simulations), a second linear trend appears that is distinctly different from the higher-temperature regime. The appearance of a second trend will be discussed further in Section 3.3.3.1.

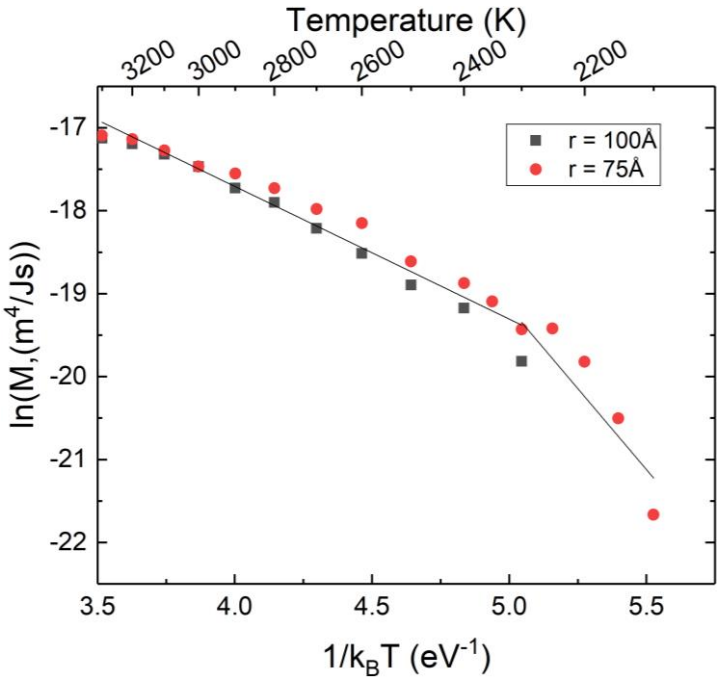

Figure 20 Temperature-dependent grain boundary mobility for the <100> 45° boundary using two initial grain radii.

As mentioned above, comparison between the r_0 = 75 Å and the r_0 = 100 Å data does not appear to reveal significant differences in the temperature range where both experience discernible grain growth for the <100> 45° boundaries. Because of this, the smaller initial radii are used to expand the range over which data has been extracted, with reasonable confidence that grain growth in the smaller grains is similar to the grain growth in the larger grains. However, in

the 20° boundaries shown later, there is a significant difference between the two radii. Thus, only the results using the r_0 = 100 Å radius will be used to compare with those of the 20° boundaries.

3.3.2.2 Periodic image interaction

One pitfall that comes with using periodic boundary conditions is that a boundary can interact with its periodic image, where in a real polycrystal, such a self-interaction is generally not expected to occur. This interaction can potentially influence the calculated grain boundary mobilities. A schematic of the grain boundary system with its periodic images is shown in Figure 21. If the distance between the actual boundary and its periodic image is small, a possibility of error is present. In this work, the boundary with the smallest distance between the real boundary and its nearest periodic image is the <110> boundary, with a minimum distance of 23 Å (approximately twice the cutoff distance used for the Buckingham and Morse potentials). The effect of the distance between the boundary and its periodic image was tested on this boundary by creating a larger crystal structure (containing approximately 256,000 atoms) with the same initial grain radius (100 Å) and calculating the mobility in the same temperature range. The separation distance between the boundary and its periodic image in the larger simulation system was approximately 100 Å. A comparison between the calculated mobilities from the two system sizes is shown in Figure 22. The calculated mobilities between the two system sizes do not differ significantly, but the larger system results in slightly lower mobilities and experiences grain growth at lower temperatures. If a smaller initial radius (75 Å) is used in the smaller system, the mobilities are closer to those in the original system. These results indicate that the small distance between the original simulation system and its periodic images may artificially increase the mobility, although the effect is not very significant.

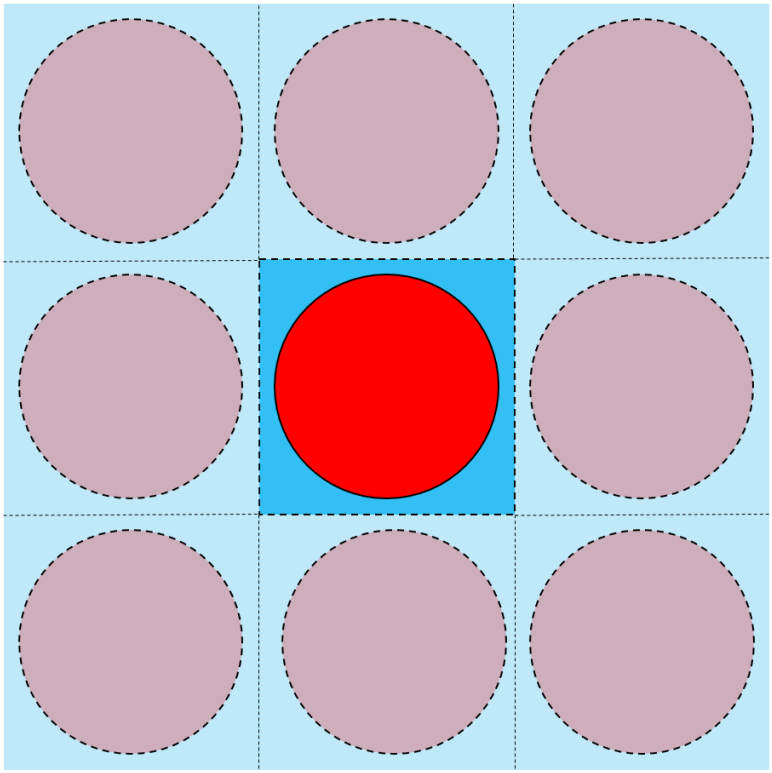

Figure 21 Schematic of the grain structure with periodic boundary conditions. If the distance between the actual grain boundary (solid line circle) and its periodic images (dashed line circles) is too small, the grain boundary migration can be impacted.

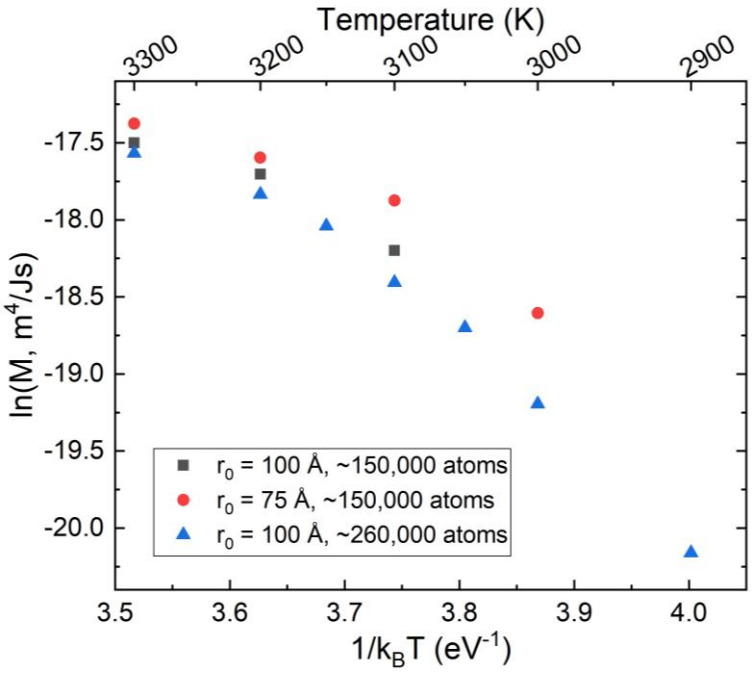

Figure 22 Comparison of the calculated mobilities from two system sizes for the <110> 45° boundary.

3.3.3 Misorientation anisotropy

In this section, only one degree of freedom is examined in detail. The inclination degrees of freedom are averaged out, leaving the three misorientation degrees of freedom. To limit this discussion to one degree of freedom, mobilities will be discussed by rotation axis, limiting the variance between the mobilities to be due to the misorientation angle (or the angle by which the cylinder was rotated).

3.3.3.1 <100> boundaries

As identified above, the <100> 45° boundary appears to have two distinct activation energy regimes when including the data from the smaller grain radius. The high-temperature regime (T > 2250 K) has a lower activation energy than the low-temperature regime. The transition between these two regimes appears to be relatively sharp. Other computational studies have found similar behaviors in fcc metals such as Cu [32, 35], Al [48], and Ni [48, 84]. The trends observed in these metals varies however. Some studies identified trends consistent with what is presented here, while others have found that a low-temperature regime has a low activation energy, and that a high-temperature regime has a high activation energy, a trend that is opposite to that presented here [48, 50, 84]. The presence of multiple regimes has not been disputed in the literature, but some research groups have found that the distinction between the two regimes becomes less pronounced as the transition regime is more densely sampled [42]. This may be indicative of a more gradual change between migration mechanisms as one (or more [44]) mechanisms become dominant at different temperatures. There is no clear reason for why there is a change, though some have postulated that it is related to a change in boundary structure, and not necessarily a change in mechanism [84]. O'Brien and Foiles [42] examined one such boundary that exhibited a sudden transition, and found that as it was more densely sampled that the transition smoothed out. Examination of the atomic motion both above and below the transition regime did not reveal any difference in mechanism, or structure. It should be noted that though no difference in mechanism or structure was found in one boundary, this is not suggestive of a general trend. As the boundaries in this work are curved, it would be difficult to determine specific structural changes due to the varying inclinations.

The <100> 20° boundary mobilities are shown in Figure 23 with the mobilities of the <100> 45° boundary for comparison. It is unclear whether the <100> 20° boundary has two distinct activation energy regimes, because the temperature range at which the transition occurred for the <100> 45° boundary could not be reached using an initial grain radius of 100 Å. There is a possibility of a transition below 2500 K, but further simulations are needed at lower temperatures to verify this. Between the two boundaries, the mobilities are roughly similar. Studies have found that as the temperature approaches the melting point of the material, the mobility of the different boundaries converges to a single value [35]. This is associated with grain boundary pre-melting. The boundaries in this work did not appear to experience a pre-melting transition, though this could be due in part to the melting temperature not being reached. At the highest temperature examined (3300 K, or ~93% of the estimated melting temperature), the <100> boundaries do not appear to approach a single mobility value, though the difference could be within the margin of error. The activation energies and mobility prefactors for these two boundaries are shown in Table 6. The <100> 45° boundary has a higher activation energy and significantly higher prefactor than the <100> 20° boundary (when comparing the high-temperature regime of the 45° boundary).

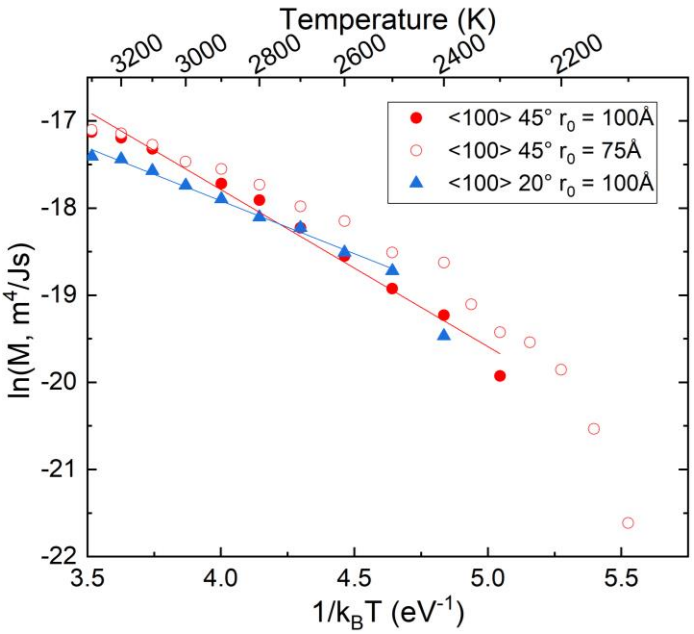

Figure 23 Arrhenius plot of the mobilities of the <100> 45° and 20° boundaries. The linear fit for the 45° boundary does not include the r_0 = 75 Å data.

3.3.3.2 <110> boundaries

Grain growth in the <110> 45° boundary was severely limited. For the system with approximately 150,000 atoms, an initial grain radius of 100 Å resulted in significant growth at temperatures from 3100 K to 3300 K. Decreasing the initial grain radius to 75Å extended grain growth to 3000 K. Using the larger system size, grain growth was observed as low as 2900 K (see Figure 22). Because of the small number of data points, it is unclear what behavior this boundary exhibits. There appears to be some curvature to the Arrhenius plot of the larger system, which will be discussed in detail in Section 3.3.3.3. One potential reason for the lack of significant growth of this boundary is the appearance of facets during grain growth at low temperatures. Early in the grain shrinkage, the structure formed facets (which appear to be oriented along <111>, <112> or <113> directions, see Figure 24). The local curvature driving force along the length of these facets is eliminated (the local radius is infinity), but the curvature near the ends of the facets would be significantly larger (the local radius is small). These facets appeared when the temperature was at or below 3000 K. Rabkin [85] examined the effect of faceting on (2D) grain growth, and determined that cusps in the grain boundary energy versus grain boundary misorientation plot lead to the formation of facets. These facets in turn slow down normal grain growth. While there does not appear to be a sharp cusp at the 45° misorientation (see Figure 12b), there is a possibility that the cylindrical grain has rotated (discussed in more detail in Section 3.3.5) to a higher misorientation to approach a <110> Σ11 boundary with a misorientation of 50.47°, which has been identified as a cusp in fcc metals [77]. It is also possible that inclinations corresponding to these facets result in cusps in grain boundary energy. Another potential reason for why the boundary did not experience grain growth was discussed by Holm and Foiles [86]. They determined that all boundaries undergo a roughening transition, and that the temperature at which this transition occurs can relate to the speed with which the boundary migrates.

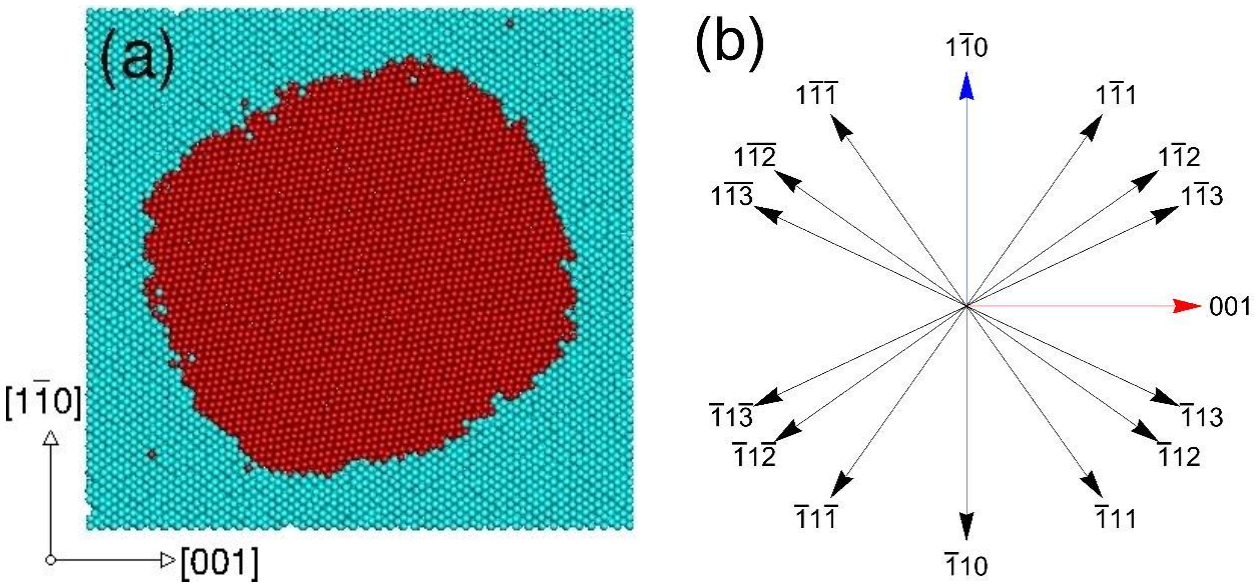

Figure 24 (a) Example of faceting in the <110> 45° boundary at T = 2700 K after 6 ns. (b) Vectors orthogonal to the [110] axis, for reference in estimating the faceting planes.

The <110> 20° boundary did not experience the same stagnation as the <110> 45° boundary. A comparison of the two boundary mobilities is shown in Figure 25. The 20° boundary is seen to be faster than the 45° boundary over the majority of the temperature range examined. As the temperature increases, the mobility is seen to converge at 3300 K, though no boundary pre-melting was observed. Both the 20° and 45° boundaries exhibited faceting behavior, though the temperature at which these facets formed for the 20° (below 2500 K) was significantly lower than the temperature for the 45° boundary (below 3000 K). It is unclear if the grain had reached stagnation at 2400 K: one of the simulations showed step-like growth, with periods of active growth, followed by periods of stagnation, while others showed relatively consistent growth (see Figure 26). This step-like behavior did not occur above 2400 K, indicating that there may exist a competition between boundary faceting and shrinking at this temperature. A comparison of the activation energies and prefactors (shown in Table 6) reveals that the 45° boundary again has a significantly higher activation energy and prefactor. The activation energy for the <110> 20° larger system (not shown in Table 6) is 2.04 eV, roughly the average between the reported values for the two misorientations. It is unclear why the larger system has a larger activation energy - further analysis is required to gain insights into this behavior. The mobility prefactor for the <110> 20° larger system is 3.9×10^{-5} m^4/Js.

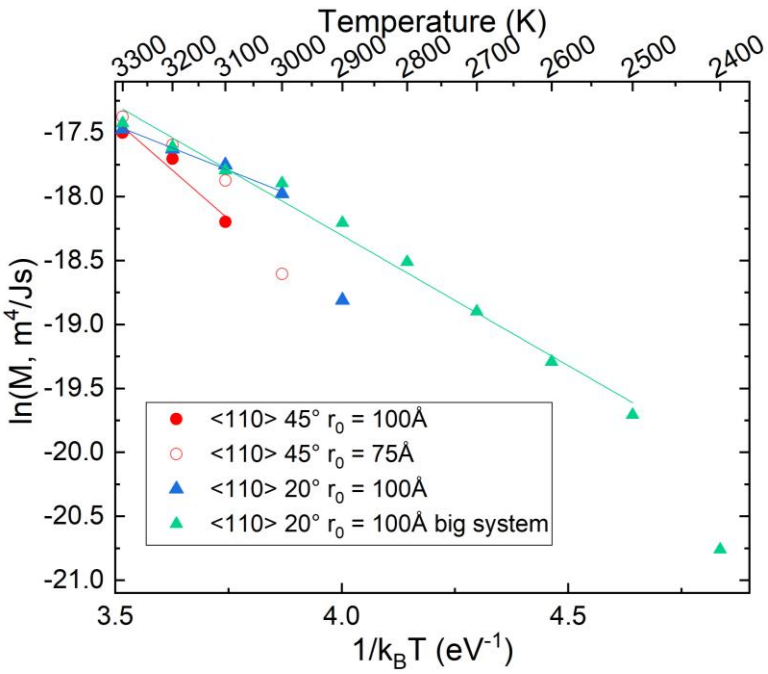

Figure 25 Arrhenius plot of the <110> 45° and 20° mobilities. Note that the big system for the 20° data has consistent mobility values with the normally sized system, but the range over which significant grain growth occurred was appreciably larger.

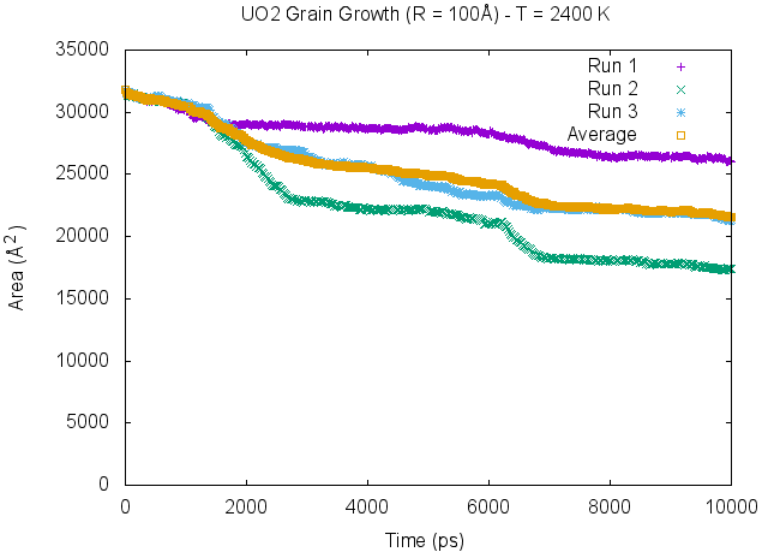

Figure 26 Example of step-like growth for the <110> 20° boundary at T = 2400 K. Note that this behavior does not always occur.

3.3.3.3 <111> boundaries

Unique to the <111> 45° boundary is an anti-thermal regime at high temperatures (T > 3000 K, see Figure 27). In this regime, an increase of temperature will cause a decrease in the mobility of the boundary, contrary to expected Arrhenius behavior. Below this regime (T < 3000 K) the Arrhenius plot shows a curvature that becomes more pronounced at the lower temperatures. A curved Arrhenius plot was interpreted by Zhang *et al*. [87] to mean that Arrhenius kinetics may not fully capture the complex temperature dependence of the grain boundary mobility. Rather, grain boundary mobilities with curved Arrhenius plots are assumed to follow the dynamics of glass-forming liquids, following the Vogel-Fulcher equation. This equation is similar to the Arrhenius equation, but uses three material-specific specific constants: M_{VF}, Q_{VF}, and T_0, representing the Vogel-Fulcher mobility prefactor, Vogel-Fulcher activation energy, and relative strength of the non-Arrhenius fit respectively. This equation is:

$$M = M_{VF} \exp\left(-\frac{Q_{VF}}{k_B (T - T_0)} \right) \tag{10}$$

By fitting the mobility data of the <111> 45° boundary to the Vogel-Fulcher equation, these material-specific constants can be extracted. This fit is shown in Figure 28, and the fitted values are shown in Table 5. The good fit demonstrates that such curvature may be due to glass-like formations at the grain boundary, though an analysis of the grain boundary structure is beyond the scope of this work. Using the Vogel-Fulcher analysis, both the activation energy and prefactor are about five times smaller than what is indicated using Arrhenius analysis.

The <111> 20° boundary did not appear to exhibit any unique characteristics, apart from the linearity of the Arrhenius plot. This in itself is unique, as none of the other boundaries appear to exhibit a strictly linear Arrhenius plot. Similar to the <110> rotation axis, the mobility appears to converge at the highest temperature. The activation energies and mobility pre-factors for both of these boundaries are given in Table 6. These boundaries exhibit an opposite trend to that observed by the <100> and <110> boundaries: the 45° boundary has a somewhat smaller activation energy and prefactor.

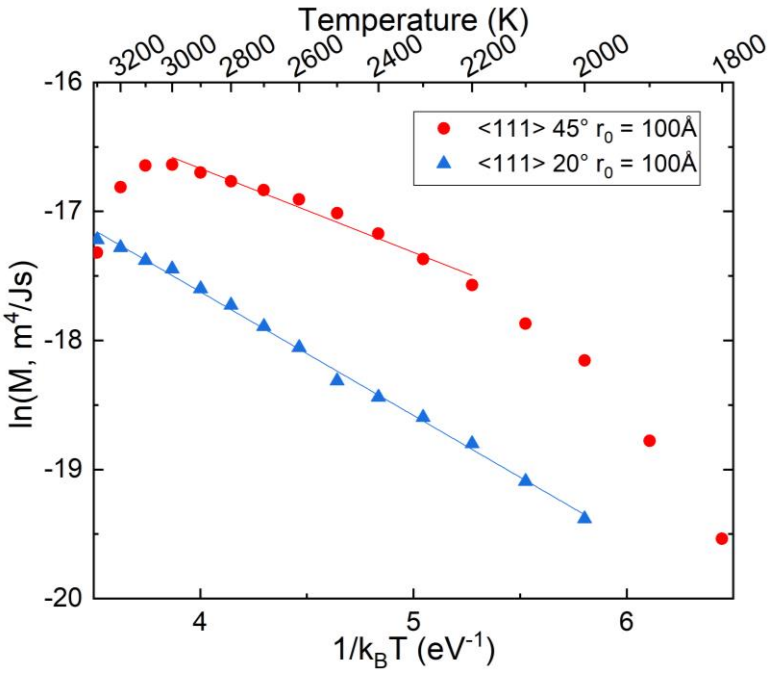

Figure 27 Arrhenius plot of the <111> 45° and 20° boundary mobilities.

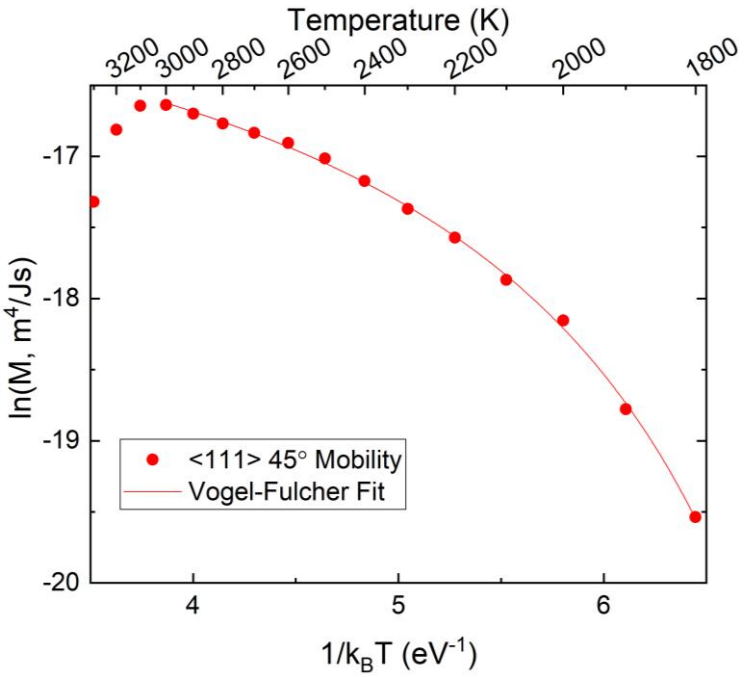

Figure 28 Arrhenius plot of the <111> 45° boundary mobilities with a Vogel-Fulcher fit.

Table 5 Fitted parameters for the Vogel-Fulcher fit shown in Figure 28.

M_{VF} (m^4/Js)	Q_{VF} (eV)	T_0 (K)
0.0149×10^{-5}	0.123	1430

Table 6 Mobility prefactor (M_0) and associated activation energy (Q_0) extracted from Arrhenius plots for the boundaries examined in this work. Note that the second values in the <100> 45° boundary column are the fit for the low-temperature regime.

Misorientation	Parameter	<100>	<110>	<111>
45°	M_0 (m^4/Js)	2.5×10^{-5} 20000	91.2×10^{-5}	0.075×10^{-5}
	Q_0 (eV)	1.80 5.6	3.1	0.65
20°	M_0 (m^4/Js)	0.2×10^{-5}	0.4×10^{-5}	0.1×10^{-5}
	Q_0 (eV)	1.21	1.4	0.96

3.3.4 Rotation axis anisotropy

This section examines the anisotropy between the rotation axes. This discussion is limited to the two degrees of freedom held constant in the discussions in the previous section, while holding the rotation angle constant.

3.3.4.1 45° boundaries

A comparison of all three 45° boundary mobilities is shown in Figure 29. As the temperature increased, the mobility seems to converge towards a single point (though the <100> 45° boundary appears to be slightly higher). Below this convergence temperature, the mobility follows the trend $M_{111} > M_{100} > M_{110}$. The mobility of the <111> boundaries was the fastest across a majority of the temperature range. This has been found both experimentally [88] and

computationally [48, 62] for Al, Cu, Au, Ni, and other fcc metals. There has been no clear reason for this behavior however. Looking at the activation energies and mobility prefactors as given in Table 6, there is a significant difference between these boundaries, though the reasons why are unclear.

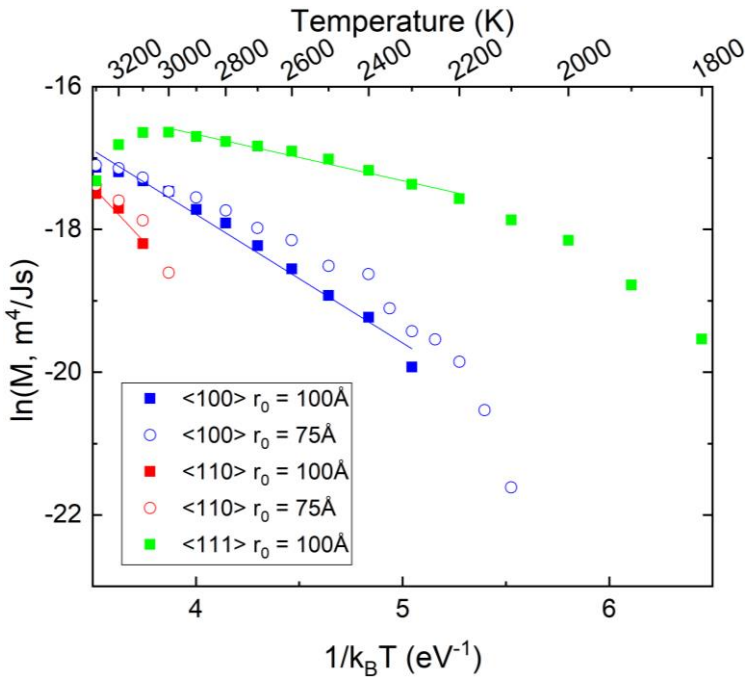

Figure 29 Arrhenius plot of the 45° boundaries for each rotation axis studied in this work.

3.3.4.2 20° boundaries

The 20° boundary mobilities are shown in Figure 30. This data set does not appear to converge to a single mobility as clearly as the 45° boundary does, though if temperatures above 3300 K were examined, it is expected that they would converge more cleanly. Again, the mobility trend for this data set is $M_{111} > M_{100} > M_{110}$, consistent with the behavior observed in the 45° boundary. A comparison of the activation energies and mobility prefactors reveals that they are very similar, perhaps indicative of a similar migration mechanism being active for this particular misorientation for any rotation axis. Further testing would be needed to validate or refute this claim however.

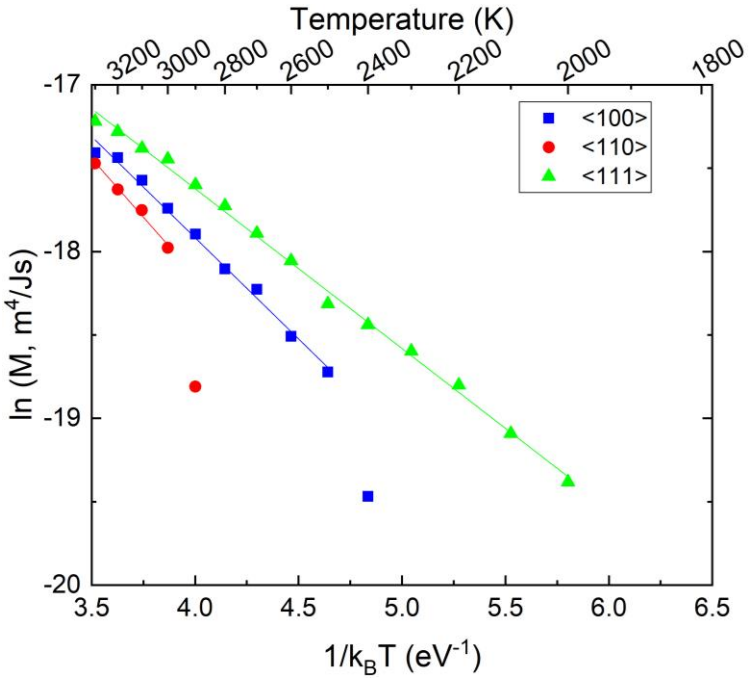

Figure 30 Arrhenius plot of the 20° boundaries for each rotation axis studied in this work.

3.3.5 Grain rotation

Grain rotation has been found to be directed towards specific angles, at least within the <100> oriented fcc metals [35]. Trautt and Mishin [35] identified the preferred misorientation angle as 36.9° for <100> oriented boundaries, which corresponds with a change in the multi-valued coupling factor for normal grain growth and grain boundary sliding. No preferred misorientation angle has been identified for <110>- or <111>-oriented grain boundaries. Grain rotation across all simulations was examined for each boundary, leading to the following results:

- <100> 45° boundaries prefer not to rotate, with approximately 65% of all simulated <100> 45° boundaries not experiencing discernible rotation. See Figure 31.
- <110> 45° boundaries prefer to rotate clockwise, with over 68% of all simulated boundaries doing so. See Figure 32.
- <111> 45° boundaries tended to experience counterclockwise rotation (approximately 75% of the simulations). See Figure 33.
- <100> 20° boundaries experienced counterclockwise rotation (85% of all simulated boundaries). See Figure 34.

- <110> 20° boundaries also experienced counterclockwise rotation (93.3%). See Figure 35.
- <111> 20° boundaries all rotated counterclockwise (100%). See Figure 36.

The temperature dependence of grain rotation varied from boundary to boundary, as some boundaries only experienced rotation at higher temperatures (inconsistent with the predictions of Trautt and Mishin [35]), while others rotated at low- to mid-temperatures. Further study is needed to understand grain rotation behavior in UO_2.

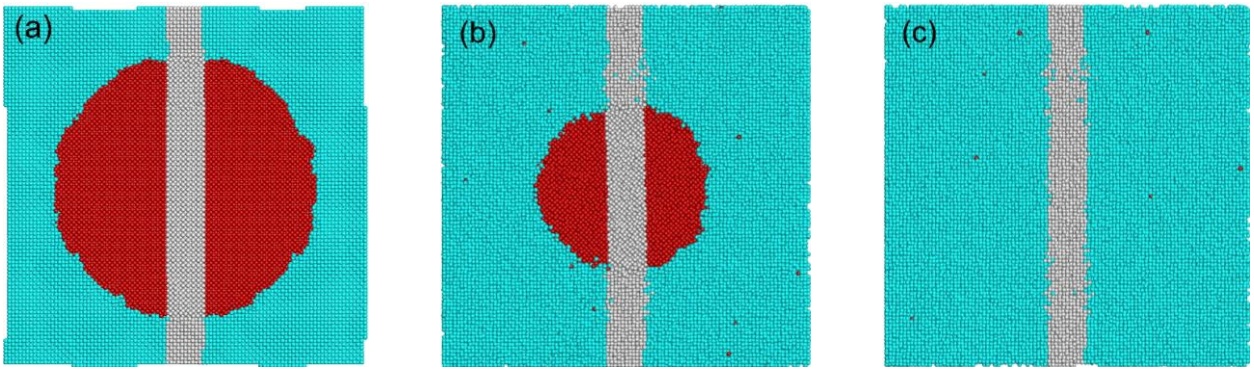

Figure 31 Example of (no) grain rotation during grain shrinkage for the <100> 45° boundary at T = 3000 K. The grey atoms are selected as "markers" to determine grain rotation. In this example, no discernible rotation was observed. (a) initial structure, (b) half-shrunk structure, (c) final structure.

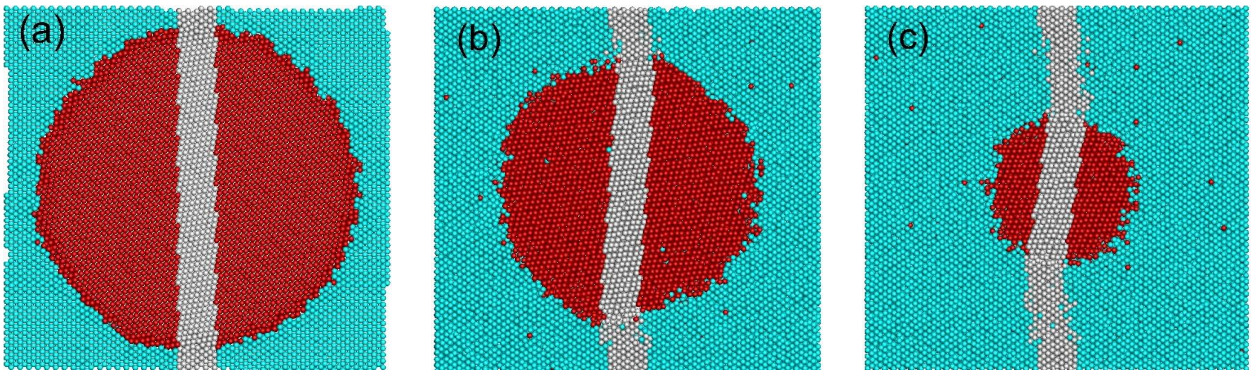

Figure 32 Example of clockwise grain rotation during grain growth for the <110> 45° boundary at T = 3200 K. (a) initial structure, (b) structure halfway through simulation, (c) final structure.

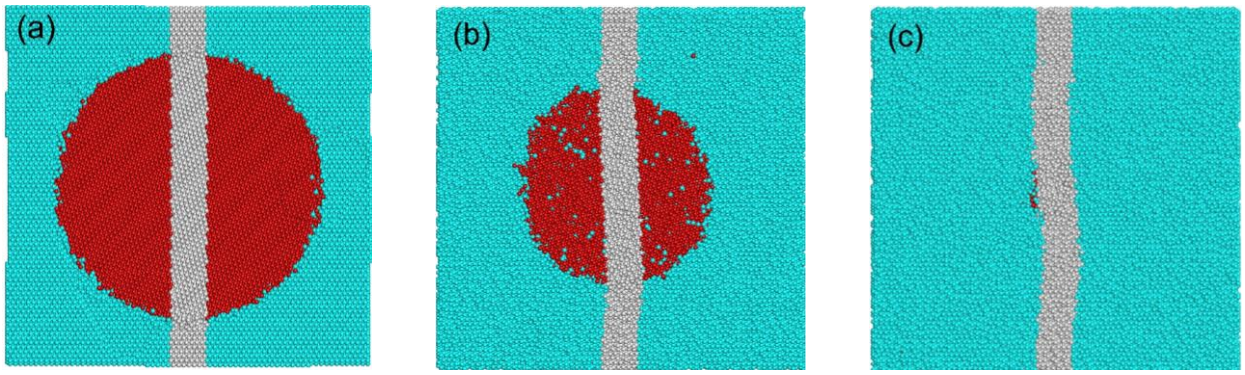

Figure 33 Example of counterclockwise grain rotation during grain growth for the <111> 45° boundary at T = 2400 K. (a) initial structure, (b) half-shrunk structure, (c) final structure.

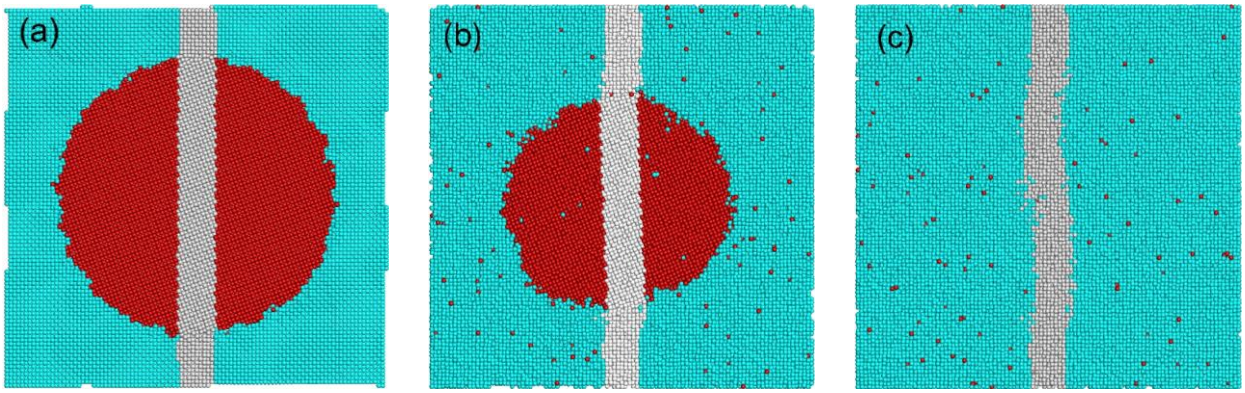

Figure 34 Example of counterclockwise grain rotation during grain growth in the <100> 20° boundary at T = 2900 K. (a) initial structure, (b) half-shrunk structure, (c) final structure.

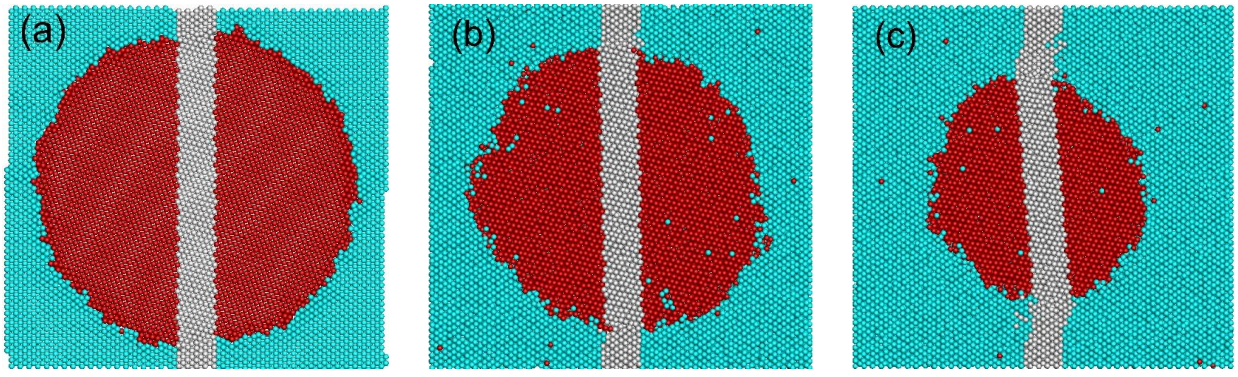

Figure 35 Example of counterclockwise rotation during grain growth in the <110> 20° boundary at T = 2900 K. (a) initial structure, (b) structure halfway through simulation, (c) final structure.

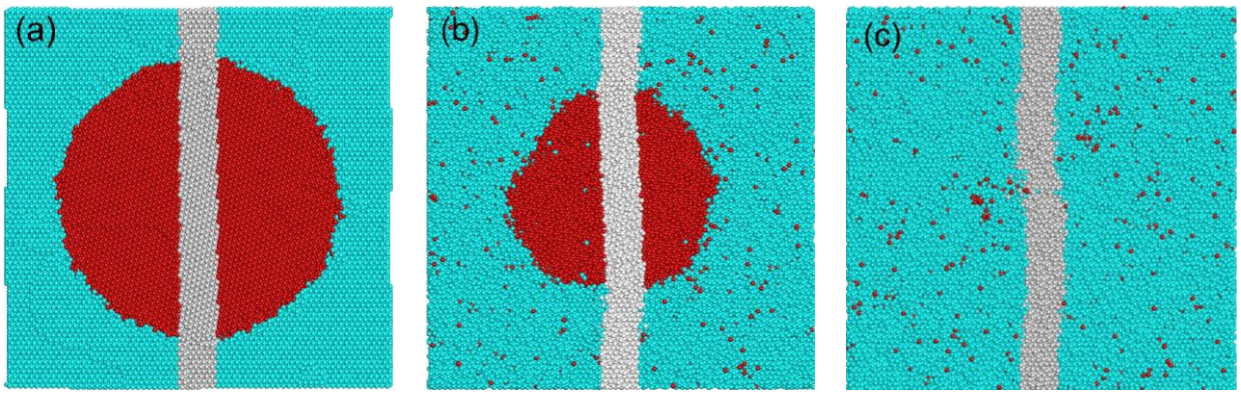

Figure 36 Example of counterclockwise rotation during grain growth in the <111> 20° boundary at T = 2900 K. (a) initial structure, (b) half-shrunk structure, (c) final structure.

Chapter 4 – CONCLUSION AND FUTURE WORK

In this work, molecular dynamics simulations have been used to study the anisotropy in grain boundary energy and mobility in UO_2, an important nuclear fuel material. The dependence of these properties on both rotation axis and misorientation angle were studied. The simulations were conducted using a cylindrical grain embedded in a matrix. It is found that grain boundary energy has a moderate anisotropy with misorientation angle and rotation axis, indicating that grain boundary energy is not a dominant factor for affecting the grain growth rate. The grain boundary mobility however, exhibits significant anisotropy for both rotation axis and misorientation angle, which is expected to affect the grain growth behavior significantly. The grain boundary energy in the high-angle regime is limited to a range between 1.5 J/m^2 and 2.0 J/m^2. The grain boundary mobility shows significant anisotropy. For both 20° and 45° misorientation angles, it has been observed that the mobility follows the trend of $M_{111} > M_{100} > M_{110}$. In particular, at the 45° misorientation this trend is pronounced. In terms of misorientation dependence, the mobilities of the 45° misorientations are higher than those of the 20° misorientation, in particular for the <111> rotation axis. Although an Arrhenius behavior of boundary mobility is assumed for data analysis, most boundary mobilities do not have perfect Arrhenius behavior with temperature. Interestingly, the <111> 45° boundary has an anti-thermal behavior at high temperatures. Additionally, this work has examined the presence of grain rotation during normal grain shrinkage. In general, most of the grain boundaries did experience grain rotation as predicted by Trautt and Mishin [35], but the <100> 45° boundary did not. The rotation can be either counterclockwise or clockwise, and the rotation behavior can change with temperature. All the results from this work indicate that grain growth in the UO_2 system is complex. Some behaviors are consistent with pure fcc metals, and some are not.

The boundaries covered here explore only a small part of grain boundary five-space, so additional work can be done to determine if additional boundaries exhibit significant anisotropy in grain boundary mobility. In nuclear fuels, grain growth is significantly affected by the presence of fission products and radiation-induced microstructures. The interaction between grain boundaries and these features, and the associated impacts on grain boundary motion, need further investigation.

References

[1] U.S. Energy Information Administration, International Energy Outlook 2017, 2017.

[2] OECD/IEA, Electricity Information: Overview, 2018.

[3] U.S. Energy Information Administration, Nuclear by the Numbers, April 2018.

[4] E.P. Steinberg, Nuclear Fission, Encyclopaedia Britannica, Inc.

[5] World Nuclear Association, Nuclear Power Reactors, 2018. (Accessed 13 February 2019).

[6] N. Touran, Nuclear Factlets. https://whatisnuclear.com/factoids.html. (Accessed 13 February 2019).

[7] M.R. Tonks, D. Andersson, S.R. Phillpot, Y. Zhang, R. Williamson, C.R. Stanek, B.P. Uberuaga, S.L. Hayes, Mechanistic materials modeling for nuclear fuel performance, Annals of Nuclear Energy 105 (2017) 11-24.

[8] D. Gaston, C. Newman, G. Hansen, D. Lebrun-Grandié, MOOSE: A parallel computational framework for coupled systems of nonlinear equations, Nuclear Engineering and Design 239(10) (2009) 1768-1778.

[9] M.R. Tonks, D. Gaston, P.C. Millett, D. Andrs, P. Talbot, An object-oriented finite element framework for multiphysics phase field simulations, Computational Materials Science 51(1) (2012) 20-29.

[10] R.L. Williamson, J.D. Hales, S.R. Novascone, M.R. Tonks, D.R. Gaston, C.J. Permann, D. Andrs, R.C. Martineau, Multidimensional multiphysics simulation of nuclear fuel behavior, Journal of Nuclear Materials 423(1) (2012) 149-163.

[11] C.B. Lee, Y.S. Yang, D.H. Kim, S.K. Kim, J.G. Bang, A New Mechanistic and Engineering Fission Gas Release Model for a Uranium Dioxide Fuel, Journal of Nuclear Science and Technology 45(1) (2008) 60-71.

[12] M.J.F. Notley, I.J. Hastings, A microstructure-dependent model for fission product gas release and swelling in UO2 fuel, Nuclear Engineering and Design 56(1) (1980) 163-175.

[13] J. Rest, M.W.D. Cooper, J. Spino, J.A. Turnbull, P. Van Uffelen, C.T. Walker, Fission gas release from UO2 nuclear fuel: A review, Journal of Nuclear Materials 513 (2019) 310-345.

[14] C.T. Walker, D. Staicu, M. Sheindlin, D. Papaioannou, W. Goll, F. Sontheimer, On the thermal conductivity of UO2 nuclear fuel at a high burn-up of around 100MWd/kgHM, Journal of Nuclear Materials 350(1) (2006) 19-39.

[15] L. Gao, B. Chen, Z. Xiao, S. Jiang, J. Yu, Pore pressure calculation of the UO2 high burnup structure, Nuclear Engineering and Design 260 (2013) 11-15.

[16] T.J. Gerczak, C.M. Parish, P.D. Edmondson, C.A. Baldwin, K.A. Terrani, Restructuring in high burnup UO2 studied using modern electron microscopy, Journal of Nuclear Materials 509 (2018) 245-259.

[17] J. Noirot, L. Desgranges, J. Lamontagne, Detailed characterisations of high burn-up structures in oxide fuels, Journal of Nuclear Materials 372(2) (2008) 318-339.

[18] V.V. Rondinella, T. Wiss, The high burn-up structure in nuclear fuel, Materials Today 13(12) (2010) 24-32.

[19] R. Yuda, H. Harada, M. Hirai, T. Hosokawa, K. Une, S. Kashibe, S. Shimizu, T. Kubo, Effects of pellet microstructure on irradiation behavior of UO2 fuel, Journal of Nuclear Materials 248 (1997) 262-267.

[20] K.A. Terrani, M. Balooch, J.R. Burns, Q.B. Smith, Young's modulus evaluation of high burnup structure in UO2 with nanometer resolution, Journal of Nuclear Materials 508 (2018) 33-39.

[21] K. Nogita, K. Une, Effect of Grain Size on Microstructural Change and Damage Recovery in UO2 Fuels Irradiated to 23 GWd/t, Journal of Nuclear Science and Technology 31(9) (1994) 929-936.

[22] I. Zacharie, S. Lansiart, P. Combette, M. Trotabas, M. Coster, M. Groos, Microstructural analysis and modelling of intergranular swelling of an irradiated UO2 fuel treated at high temperature, Journal of Nuclear Materials 255(2) (1998) 92-104.

[23] J.A. Turnbull, C.A. Friskney, The relation between microstructure and the release of unstable fission products during high temperature irradiation of uranium dioxide, Journal of Nuclear Materials 71(2) (1978) 238-248.

[24] K. Momma, F. Izumi, VESTA 3 for three-dimensional visualization of crystal, volumetric and morphology data, Journal of Applied Crystallography 44(6) (2011) 1272-1276.

[25] G. Gottstein, L.S. Shvindlerman, Grain boundary migration in metals: thermodynamics, kinetics, applications, CRC press2009.

[26] A.P. Sutton, R.W. Balluffi, Interfaces in crystalline materials, Clarendon Press, Oxford, 1995.

[27] S.M. Foiles, J.J. Hoyt, Computation of grain boundary stiffness and mobility from boundary fluctuations, Acta Materialia 54(12) (2006) 3351-3357.

[28] D.L. Olmsted, S.M. Foiles, E.A. Holm, Survey of computed grain boundary properties in face-centered cubic metals: I. Grain boundary energy, Acta Materialia 57(13) (2009) 3694-3703.

[29] D.L. Olmsted, E.A. Holm, S.M. Foiles, Survey of computed grain boundary properties in face-centered cubic metals—II: Grain boundary mobility, Acta Materialia 57(13) (2009) 3704-3713.

[30] M. Upmanyu, D.J. Srolovitz, L.S. Shvindlerman, G. Gottstein, Misorientation dependence of intrinsic grain boundary mobility: simulation and experiment, Acta Materialia 47(14) (1999) 3901-3914.

[31] H. Zhang, M. Upmanyu, D.J. Srolovitz, Curvature driven grain boundary migration in aluminum: molecular dynamics simulations, Acta Materialia 53(1) (2005) 79-86.

[32] B. Schönfelder, G. Gottstein, L.S. Shvindlerman, Comparative study of grain-boundary migration and grain-boundary self-diffusion of [001] twist-grain boundaries in copper by atomistic simulations, Acta Materialia 53(6) (2005) 1597-1609.

[33] Y. Mishin, M. Asta, J. Li, Atomistic modeling of interfaces and their impact on microstructure and properties, Acta Materialia 58(4) (2010) 1117-1151.

[34] B. Schönfelder, G. Gottstein, L.S. Shvindlerman, Atomistic simulations of grain boundary migration in copper, Metallurgical and Materials Transactions A 37(6) (2006) 1757-1771.

[35] Z.T. Trautt, Y. Mishin, Grain boundary migration and grain rotation studied by molecular dynamics, Acta Materialia 60(5) (2012) 2407-2424.

[36] A.T. Wicaksono, C.W. Sinclair, M. Militzer, An atomistic study of the correlation between the migration of planar and curved grain boundaries, Computational Materials Science 117 (2016) 397-405.

[37] H. Zhang, M.I. Mendelev, D.J. Srolovitz, Mobility of Σ5 tilt grain boundaries: Inclination dependence, Scripta Materialia 52(12) (2005) 1193-1198.

[38] J.E. Brandenburg, L.A. Barrales-Mora, D.A. Molodov, On migration and faceting of low-angle grain boundaries: Experimental and computational study, Acta Materialia 77 (2014) 294-309.

[39] A. Vuppuluri, Theory and simulation of microstructure evolution due to simultaneous grain boundary migration and grain rotation with misorientation dependent energy and mobility, Materials Science and Engineering: A 713 (2018) 118-124.

[40] M. Upmanyu, G.N. Hassold, A. Kazaryan, E.A. Holm, Y. Wang, B. Patton, D.J. Srolovitz, Boundary Mobility and Energy Anisotropy Effects on Microstructural Evolution During Grain Growth, Interface Science 10(2) (2002) 201-216.

[41] I. Toda-Caraballo, P.D. Bristowe, C. Capdevila, A molecular dynamics study of grain boundary free energies, migration mechanisms and mobilities in a bcc Fe–20Cr alloy, Acta Materialia 60(3) (2012) 1116-1128.

[42] C.J. O'Brien, S.M. Foiles, Exploration of the mechanisms of temperature-dependent grain boundary mobility: search for the common origin of ultrafast grain boundary motion, Journal of Materials Science 51(14) (2016) 6607-6623.

[43] R.-J. Jhan, P.D. Bristowe, A molecular dynamics study of grain boundary migration without the participation of secondary grain boundary dislocations, Scripta Metallurgica et Materialia 24(7) (1990) 1313-1318.

[44] F. Ulomek, V. Mohles, Separating grain boundary migration mechanisms in molecular dynamics simulations, Acta Materialia 103 (2016) 424-432.

[45] W. Rheinheimer, M.J. Hoffmann, Non-Arrhenius behavior of grain growth in strontium titanate: New evidence for a structural transition of grain boundaries, Scripta Materialia 101 (2015) 68-71.

[46] Y. Huang, F.J. Humphreys, Subgrain growth and low angle boundary mobility in aluminium crystals of orientation {110}〈001〉, Acta Materialia 48(8) (2000) 2017-2030.

[47] I. Chesser, E. Holm, Understanding the anomalous thermal behavior of Σ3 grain boundaries in a variety of FCC metals, Scripta Materialia 157 (2018) 19-23.

[48] C. Deng, C.A. Schuh, Atomistic Simulation of Slow Grain Boundary Motion, Physical Review Letters 106(4) (2011) 045503.

[49] P.R. Cantwell, E.A. Holm, M.P. Harmer, M.J. Hoffmann, Anti-thermal behavior of materials, Scripta Materialia 103 (2015) 1-5.

[50] E.R. Homer, E.A. Holm, S.M. Foiles, D.L. Olmsted, Trends in Grain Boundary Mobility: Survey of Motion Mechanisms, Journal of the Minerals, Metals & Materials Society 66(1) (2014) 114-120.

[51] S. Logan, The origin and status of the Arrhenius equation, Journal of Chemical Education 59(4) (1982) 279.

[52] P. Lejček, Grain Boundaries: Description, Structure and Thermodynamics, in: P. Lejcek (Ed.), Grain Boundary Segregation in Metals, Springer Berlin Heidelberg, Berlin, Heidelberg, 2010, pp. 5-24.

[53] M. Winning, G. Gottstein, L.S. Shvindlerman, On the mechanisms of grain boundary migration, Acta Materialia 50(2) (2002) 353-363.

[54] M. Upmanyu, R.W. Smith, D.J. Srolovitz, Atomistic Simulation of Curvature Driven Grain Boundary Migration, Interface Science 6(1) (1998) 41-58.

[55] M. Upmanyu, D.J. Srolovitz, A.E. Lobkovsky, J.A. Warren, W.C. Carter, Simultaneous grain boundary migration and grain rotation, Acta Materialia 54(7) (2006) 1707-1719.

[56] M.I. Mendelev, C. Deng, C.A. Schuh, D.J. Srolovitz, Comparison of molecular dynamics simulation methods for the study of grain boundary migration, Modelling and Simulation in Materials Science and Engineering 21(4) (2013) 045017.

[57] X.-M. Bai, Y. Zhang, M.R. Tonks, Testing thermal gradient driving force for grain boundary migration using molecular dynamics simulations, Acta Materialia 85 (2015) 95-106.

[58] M. Stan, Discovery and design of nuclear fuels, Materials Today 12(11) (2009) 20-28.

[59] J.R. MacEwan, Grain Growth in Sintered Uranium Dioxide: I, Equiaxed Grain Growth, Journal of the American Ceramic Society 45(1) (1962) 37-41.

[60] J.R. MacEwan, V.B. Lawson, Grain Growth in Sintered Uranium Dioxide: II, Columnar Grain Growth, Journal of the American Ceramic Society 45(1) (1962) 42-46.

[61] J.B. Ainscough, B.W. Oldfield, J.O. Ware, Isothermal grain growth kinetics in sintered UO2 pellets, Journal of Nuclear Materials 49(2) (1973) 117-128.

[62] A.D. Rollett, G. Gottstein, L.S. Shvindlerman, D.A. Molodov, Grain boundary mobility – a brief review, Zeitschrift für Metallkunde 95(4) (2004) 226-229.

[63] S. Plimpton, Fast Parallel Algorithms for Short-Range Molecular Dynamics, Journal of Computational Physics 117(1) (1995) 1-19.

[64] C.B. Basak, A.K. Sengupta, H.S. Kamath, Classical molecular dynamics simulation of UO2 to predict thermophysical properties, 360(1-2) (2003) 210-216.

[65] K. Govers, S. Lemehov, M. Hou, M. Verwerft, Comparison of interatomic potentials for UO2. Part I: Static calculations, Journal of Nuclear Materials 366(1) (2007) 161-177.

[66] S.I. Potashnikov, A.S. Boyarchenkov, K.A. Nekrasov, A.Y. Kupryazhkin, High-precision molecular dynamics simulation of UO2–PuO2: Pair potentials comparison in UO2, Journal of Nuclear Materials 419(1) (2011) 217-225.

[67] B.A. Luty, M.E. Davis, I.G. Tironi, W.F. Van Gunsteren, A Comparison of Particle-Particle, Particle-Mesh and Ewald Methods for Calculating Electrostatic Interactions in Periodic Molecular Systems, Molecular Simulation 14(1) (1994) 11-20.

[68] T.C. EHLERT, J.L. MARGRAVE, Melting point and spectral emissivity of uranium dioxide, Journal of the American Ceramic Society 41(8) (1958) 330-330.

[69] K. Govers, S. Lemehov, M. Hou, M. Verwerft, Comparison of interatomic potentials for UO2: Part II: Molecular dynamics simulations, Journal of Nuclear Materials 376(1) (2008) 66-77.

[70] H. Ogawa, GBstudio: A Builder Software on Periodic Models of CSL Boundaries for Molecular Simulation, Materials Transactions 47(11) (2006) 2706-2710.

[71] H. Ogawa, GBStudio (Java applet), 2003. https://staff.aist.go.jp/h.ogawa/GBstudio/

[72] E. Polak, G. Ribiere, Note sur la convergence de méthodes de directions conjuguées, ESAIM: Mathematical Modelling and Numerical Analysis-Modélisation Mathématique et Analyse Numérique 3(R1) (1969) 35-43.

[73] S. Nosé, A unified formulation of the constant temperature molecular dynamics methods, The Journal of Chemical Physics 81(1) (1984) 511-519.

[74] S. Nosé, A molecular dynamics method for simulations in the canonical ensemble, Molecular Physics 52(2) (1984) 255-268.

[75] W.G. Hoover, Canonical dynamics: Equilibrium phase-space distributions, Physical Review A 31(3) (1985) 1695-1697.

[76] A. Stukowski, Visualization and analysis of atomistic simulation data with OVITO–the Open Visualization Tool, Modelling and Simulation in Materials Science and Engineering 18(1) (2009) 015012.

[77] V.V. Bulatov, B.W. Reed, M. Kumar, Grain boundary energy function for fcc metals, Acta Materialia 65 (2014) 161-175.

[78] A.S. Butterfield, Exploration of the phase field framework MARMOT to include anisotropic grain boundaries with molecular dynamics, Physics, Brigham Young University-Idaho, 2013.

[79] T. Harbison, Anisotropic grain boundary energy function for uranium dioxide, Physics, Brigham Young University-Idaho, 2015.

[80] J.-M.H. Bradley, Foundation for an Anisotropic Model, Physics, Brigham Young University-Idaho, 2016.

[81] J. French, Improving the Function for Grain Boundary Energy Interpolation in Uranium Dioxide, Physics, BYU-Idaho, 2016.

[82] J. Tolliver, Incorporating Anisotropic Grain Boundary Energy into a Phase Field Model of Uranium Dioxide, Physics, Brigham Young University-Idaho, 2016.

[83] C.M. Williams, A Model for Grain Boundary Energies in Uranium Dioxide, Physics, Brigham Young University-Idaho, 2018.

[84] C. Deng, C.A. Schuh, Diffusive-to-ballistic transition in grain boundary motion studied by atomistic simulations, Physical Review B 84(21) (2011) 214102.

[85] E. Rabkin, Effect of grain boundary faceting on kinetics of grain growth and microstructure evolution, Journal of Materials Science 40(4) (2005) 875-879.

[86] E.A. Holm, S.M. Foiles, How Grain Growth Stops: A Mechanism for Grain-Growth Stagnation in Pure Materials, Science 328(5982) (2010) 1138.

[87] H. Zhang, D.J. Srolovitz, J.F. Douglas, J.A. Warren, Grain boundaries exhibit the dynamics of glass-forming liquids, Proceedings of the National Academy of Sciences 106(19) (2009) 7735.

[88] Y. Huang, F.J. Humphreys, Measurements of grain boundary mobility during recrystallization of a single-phase aluminium alloy, Acta Materialia 47(7) (1999) 2259-2268.